Chapter 7
Principles of Coarse-Graining and Coupling Using the Atom-to-Continuum Method

Reese E. Jones, Jeremy Templeton, and Jonathan Zimmerman

7.1 Introduction

Molecular dynamics (MD) and finite element (FE) simulation are both powerful, widely applied methods in their own right. MD enables the study of the atomic motion that underlies material deformation and failure mechanisms. It has been a tool in understanding phenomena such as diffusion, energy transport, and fracture at a fundamental level. In contrast, FE simulation of continuum processes uses preconceived knowledge about mechanisms, in the form of constitutive models, to predict the response of structures and devices that span from microns to meters. Just as each method possesses unique strengths, they also have their limits. Typically, MD cannot be used to simulate even microscopic devices due to computational inefficiencies of resolving atomic motion at that scale, whereas FE relies heavily on phenomenological constitutive models that may not encompass all the mechanisms needed for predictive simulation.

To provide a tool to simulate and design nanoscale devices and nanostructured materials, we have developed a suite of numerical methods that bring together the best aspects of MD and FE. This coupling of methods enables us to capture multiscale phenomena [1–3], reduce atomic data to connect with continuum theory [4–7], simulate large systems with atomic detail and statistical characterization [8, 9], and add physics not intrinsic to MD [10]. In general, the methods rely on the fact that atomistic behavior is asymptotic to continuum, which is the basis for Green–Kubo methods [3] for example, and that the scales at which the two representations of materials become consistent are surprisingly short and small [11, 12].

R.E. Jones (✉) • J. Templeton • J. Zimmerman
Sandia National Laboratories, Livermore, CA, USA
e-mail: rjones@sandia.gov; jatempl@sandia.gov; jzimmer@sandia.gov

© Springer International Publishing Switzerland (outside the USA) 2016

C.R. Weinberger, G.J. Tucker (eds.), *Multiscale Materials Modeling for Nanomechanics*, Springer Series in Materials Science 245,
DOI 10.1007/978-3-319-33480-6_7

In this chapter, we review our approaches for both coarse-graining (the averaging of MD-level quantities to inform models used within FE) and coupling (concurrent simulation at the MD and FE levels such that information is exchanged through interface conditions) that have been implemented in the Atom-to-Continuum (AtC) user module available with the widely used, large-scale molecular simulation code LAMMPS [13]. As we will discuss, coupling generally involves four ingredients: (a) consistent upscaling/coarse-graining of atomic data, (b) multiscale governing balances connecting atomic and continuum representations, (c) consistent continuum constitutive models, and (d) atomistic control schemes to effect the influence of the continuum on the atomistic representation.

In the next section, Sect. 7.2, we will develop a means of coarse-graining of atomic data into continuum fields that is consistent with accepted conservation laws. Then, we will revisit (a) and cover (b)–(d) in Sect. 7.3. Finally, in Sect. 7.4 we will show examples of both coarse-graining and coupling that demonstrate the utility and versatility of these techniques. We refer the reader to Fig. 7.1 for a guide to the notation and basic geometry used in this chapter.

t	time
$\mathbf{x}$	current position
$\mathbf{X}$	reference position
$\mathbf{u}$	displacement
$\mathbf{v}$	velocity
q	charge
ζ	charge density
m	mass
ϱ	mass density
ρ	reference mass density
$\mathbf{p}$	momentum density
$\boldsymbol{\sigma}$	Cauchy stress
$\mathbf{S}$	first Piola-Kirchhoff stress
$\boldsymbol{\varsigma}$	spatial heat flux
$\mathbf{q}$	referential heat flux
Φ	potential energy
e	total energy density
ϵ	internal energy density
T	temperature

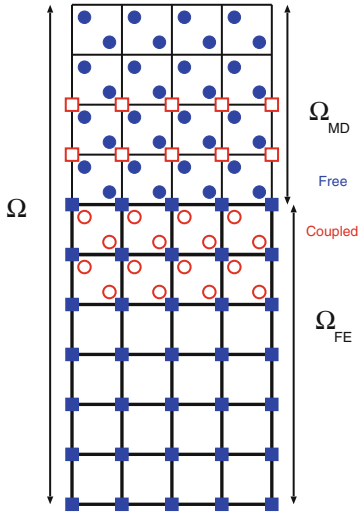

Fig. 7.1 Notation used for physical properties and fields within this chapter. Atomic quantities are indexed with Greek α subscripts and nodal/continuum fields with Latin I subscripts and unless explicitly noted α ranges over the whole set of atoms $\mathscr{A}$ and I ranges over all nodes $\mathscr{N}$. The schematic shows the finite element Ω_{FE} and molecular dynamic Ω_{MD} regions comprising the complete system $\Omega = \Omega_{\mathrm{FE}} \cup \Omega_{\mathrm{MD}}$. The nodes and atoms that are *free* evolve according to their own constitutive models reside in Ω_{FE} and Ω_{MD}, respectively, and those that are *coupled* to the other paradigm reside in Ω_{MD} and Ω_{FE}, respectively

7.2 Coarse Graining

Coarse-graining is the averaging of atomic-scale quantities in order to estimate fields that have well-defined physical meaning at larger scales. These continuum fields can be used to interpret atomistic data and construct constitutive models that guide FE simulations, or to provide interface conditions for concurrent MD/FE simulations. The development of expressions to calculate continuum fields from pointwise atomistic information dates back to the late nineteenth century, when Clausius [14] and Maxwell [15] developed the virial theorem (VT) to define the stress applied to the bounding surface of a fixed volume containing interacting particles at finite temperature. In 1950, Irving and Kirkwood [16] derived expressions for local measures of stress and heat flux from microscopic/atomic densities for mass, momentum and energy and the associated continuum balance equations.

Subsequent to these foundations, there have been many efforts to improve on atomic-based definitions for stress [4, 17–38] and heat flux [35, 38]. We direct the reader to [4, 35–37] for more complete discussions of these derivations. Notable among these efforts is the work by Hardy and colleagues [21, 39, 40] which replaced the Dirac delta employed by Irving and Kirkwood with a more computationally amenable smooth, finite localization function to establish a self-consistent manner of distributing discrete atomic contributions to thermomechanical fields. Hardy's original formulation is based on an Eulerian/spatial representation where localization volumes are essentially control volumes fixed in space that matter occupies at a particular time. Hence, as was the case for the expressions by Irving and Kirkwood [16], Hardy's expressions for (Cauchy) stress, $\boldsymbol{\sigma}$, and heat flux, $\boldsymbol{\varsigma}$, contain both potential and kinetic terms.

A Lagrangian/material frame representation affords an alternative approach particularly suited to solids and tracking *material* motion from a continuum perspective. In this case, the first Piola–Kirchhoff stress tensor $\mathbf{S}$, the amount of current force exerted on a unit area as measured in the reference configuration, is the relevant stress measure. The material frame heat flux, $\mathbf{q}$, has a similar definition and has units of energy per time per unit reference area. Expressions to calculate $\mathbf{S}$ and $\mathbf{q}$ have been developed by Andia et al. [29–32], and more recently by Zimmerman et al. [36] who used a Hardy-like formalism.

In this section, we present a generalized weighted-residual formulation for coarse-graining atomic data. We derive consistent fields from minimizing the L^2 norm of the difference between an atomic-based description of a continuum field variable and a representation using nodal variables and FE basis functions. We compare this approach with expressions developed by Irving and Kirkwood, Hardy and similar efforts found in the literature, and elucidate their connections as well as their differences. Lastly, although becoming prominent in recent research [41, 42] we do not cover the uncertainty quantification (UQ) aspects of parameter and property estimation in this chapter nor give an extensive treatment of measuring or coupling to the scale-dependent fluctuations intrinsic in MD [43].

7.2.1 Formulation

As in [44], we take a least squares statement:

$$\min_{\varrho_I} \int_\Omega \|\varrho^* - \sum_I N_I \varrho_I\|^2 \, \mathrm{d}V \Longleftrightarrow \sum_J \left[\int_\Omega N_I N_J \, \mathrm{d}V \right] \varrho_J = \int_\Omega N_I \varrho \, \mathrm{d}V \tag{7.1}$$

as starting point to relate, in this case, the mass density ϱ^* to its approximation $\sum_I N_I(\mathbf{x})\varrho_I(t)$ with a basis $\{N_I(\mathbf{x})\}$ covering region $\Omega \equiv \Omega_{\mathrm{MD}}$ filled with atoms. This is a sub-case of the more general scenario shown in Fig. 7.1.

As in Irving and Kirkwood's seminal work [16], we form microscopic densities, e.g.,

$$\varrho^*(\mathbf{x}, t) = \sum_\alpha m_\alpha \delta(\mathbf{x} - \mathbf{x}_\alpha(t)) \tag{7.2}$$

in terms of atomic quantities, here m_α is the mass of atom α, and δ is the Dirac delta operator. Hence Eq. (7.1) becomes

$$\sum_J \underbrace{\left[\int_\Omega N_I N_J \, \mathrm{d}V \right]}_{M_{IJ}} \varrho_J = \sum_\alpha N_I(\mathbf{x}_\alpha) m_\alpha = \sum_\alpha N_{I\alpha} m_\alpha \tag{7.3}$$

where $N_{I\alpha} = N_I(\mathbf{x}_\alpha)$ is the basis evaluated at atomic positions. The solution of Eq. (7.3) is the projection

$$\varrho_I = \sum_{J,\alpha} M_{IJ}^{-1} N_{J\alpha} m_\alpha = \sum_\alpha \Delta_{I\alpha} m_\alpha, \tag{7.4}$$

given the mass matrix M_{IJ}, and introduce the localization function $\Delta_I = \sum_J M_{IJ}^{-1} N_J$, with $\Delta_{I\alpha} = \Delta_I(\mathbf{x}_\alpha)$, which has units of inverse volume [45]. We can reduce this projection to a *restriction*

$$\varrho_I \approx \sum_\alpha \frac{1}{V_I} N_{I\alpha} m_\alpha = \sum_\alpha \Delta_{I\alpha} m_\alpha \tag{7.5}$$

by row-sum lumping the mass matrix $M_{IJ} \approx \sum_J M_{IJ} = \int_\Omega N_I \, \mathrm{d}V = V_I$ using the partition of unity property $\sum_I N_I = 1$ of the basis N_I, which localizes the influence of atomic data on specific nodes. In this case, $\Delta_{I\alpha} = N_{I\alpha}/V_I$. In a similar fashion, we can take the localization function to be a moving least squares (MLS) kernel [46] like in Hardy's work [21, 39, 47] so that $\Delta_{I\alpha} = \Delta(\mathbf{x}_I - \mathbf{x}_\alpha)$ with the normalization $\int_\Omega \Delta \, \mathrm{d}V = 1$, or a reproducing kernel [48] which is polynomially complete. Using either a projection (7.4), a restriction (7.5) or a moving least squares estimate to obtain nodal values, the continuum field is then interpolated using the basis

$$\varrho(\mathbf{x}, t) = \sum_I N_I(\mathbf{x}) \varrho_I(t) = \sum_{I,\alpha} N_I(\mathbf{x}) \Delta_I(\mathbf{x}_\alpha(t)) m_\alpha. \tag{7.6}$$

Note that N_I will always denote the chosen basis but the particular form of the localization Δ_I will depend on the appropriate mass matrix, which we will assume is implicit in the context of particular Δ_I.

Two characteristic sizes have been introduced into our formulation: (a) the nodal spacing of the mesh used (i.e., the scale of the basis $N_I \sim \sqrt[3]{V_I}$), which dictates the spatial refinement of our coarse-grained field, and (b) the size of the region over which averaging is performed at each node (i.e., the scale of Δ_I). These two length-scales are independent, but typically the averaging region is taken to be commensurate with the mesh spacing for convenience. This practice becomes problematic in certain cases. For example, the anticipation of large gradients may require a fine mesh; however, too fine a mesh will result in nodal averages that depend on only a few atoms. Conversely, too coarse a mesh will result in averages that are limited in their spatial variation. Alternatively, one can separate these two length-scales, using a larger size for atomic averaging and a smaller one for mesh definition,[1] as we demonstrate in the example presented in Sect. 7.4.1. Instead of a completely empirical approach, the asymptotic analysis of Ulz et al. can be employed to balance smoothness and resolution of the estimate [49].

Taking the (partial) time derivative of Eq. (7.1)

$$\sum_J \left[\int_\Omega N_I N_J \, \mathrm{d}V \right] \frac{\partial}{\partial t} \varrho_J = - \sum_\alpha \nabla_{\mathbf{x}} N_{I\alpha} \cdot m_\alpha \mathbf{v}_\alpha \tag{7.7}$$

using the short-hand

$$\frac{\partial}{\partial t} N_{I\alpha}(t) = \frac{\partial}{\partial t} N_I(\mathbf{x}_I - \mathbf{x}_\alpha(t)) = -\nabla_{\mathbf{x}} N_{I\alpha} \cdot \mathbf{v}_\alpha \tag{7.8}$$

for the application of the necessary chain rule, we see the estimates are consistent with the usual continuum Eulerian/spatial mass balance

$$\frac{\partial}{\partial t} \varrho_I + \nabla_{\mathbf{x}} \cdot \mathbf{p}_I = \dot{\varrho}_I + \varrho_I \nabla_{\mathbf{x}} \cdot \mathbf{v}_I = 0 \tag{7.9}$$

at the nodes. Here we introduce the material time derivative $\dot{\varrho} = \frac{\partial}{\partial t} \varrho + \nabla_{\mathbf{x}} \varrho \cdot \mathbf{v}$ of ϱ and the linear momentum density field $\mathbf{p} = \rho \mathbf{v}$. This approach gives an explicit sense of scale at which the estimated fields are consistent with the appropriate balance in contrast with MLS/Hardy approach [21] where at any point

$$\frac{\partial \varrho}{\partial t} = \frac{\partial}{\partial t} \sum_\alpha \Delta(\mathbf{x} - \mathbf{x}(t)) m_\alpha = - \sum_\alpha \nabla_{\mathbf{x}} \Delta(\mathbf{x} - \mathbf{x}(t)) \cdot m_\alpha \mathbf{v}_\alpha = -\nabla_{\mathbf{x}} \cdot \mathbf{p} \tag{7.10}$$

[1] This choice has similarities with the Bubnov–Galerkin weighted residual where the weight space and primary field have different bases.

The Lagrangian mass balance is trivially satisfied by

$$\rho = \sum_I N_I(\mathbf{X})\rho_I = \sum_{I,\alpha} N_I \Delta_I(\mathbf{X}_\alpha) m_\alpha \tag{7.11}$$

since $\dot{\rho}_I = 0$.

A further generalization is to introduce time averaging by revisiting the microscopic density Eq. (7.2)

$$\varrho^*(\mathbf{x}, t) = \sum_\alpha \langle m_\alpha \delta(\mathbf{x} - \mathbf{x}_\alpha(t)) \rangle \tag{7.12}$$

using a causal time-filter

$$f(t) \equiv \int_{-\infty}^{t} f(s) w(t-s)\, \mathrm{d}s. \tag{7.13}$$

The kernel $w(t)$ must asymptote to zero as $t \to -\infty$ sufficiently fast for the integral to converge, which, in conjunction with the properties of the convolution operator (7.13),[2] results in this time-average having the commutation property

$$\frac{\partial}{\partial t} \langle f \rangle = \left\langle \frac{\partial}{\partial t} f \right\rangle. \tag{7.14}$$

Thus, the time derivative of Eq. (7.1) becomes

$$\begin{aligned} \sum_J \left[\int_\Omega N_I N_J \, \mathrm{d}V \right] \frac{\partial}{\partial t} \varrho_J &= \frac{\partial}{\partial t} \left\langle \sum_\alpha N_{I\alpha} m_\alpha \right\rangle = \left\langle \sum_\alpha \frac{\partial}{\partial t} N_{I\alpha} m_\alpha \right\rangle \\ &= -\left\langle \sum_\alpha \nabla_{\mathbf{x}} N_{I\alpha} \cdot m_\alpha \mathbf{v}_\alpha \right\rangle = -\nabla_{\mathbf{x}} \cdot \left\langle \sum_\alpha N_{I\alpha} m_\alpha \mathbf{v}_\alpha \right\rangle \end{aligned} \tag{7.15}$$

and hence the time averaged definition of ϱ also satisfies the (weak) mass balance. Given the extent of the kernel into the past, which allows the filter to be invertible, means of initializing the causal filter with consistent initial conditions at some finite

[2] Using Leibniz's rule and $w(t) = 0 \forall t > 0$:

$$\begin{aligned} \frac{\partial}{\partial t} \langle f \rangle &= \frac{\partial}{\partial t} \int_{-\infty}^{t} f(s) w(t-s)\, \mathrm{d}s = -\frac{\partial}{\partial t} \int_{-\infty}^{t} f(t-s) w(s)\, \mathrm{d}s \\ &= -\int_{-\infty}^{t} \frac{\partial}{\partial t} f(t-s) w(s)\, \mathrm{d}s - \varrho(0) w(t) = -\int_{-\infty}^{t} \frac{\partial}{\partial t} f(t-s) w(s)\, \mathrm{d}s = \left\langle \frac{\partial}{\partial t} f \right\rangle \end{aligned}$$

for $t > 0$.

time are necessary [9]. With an exponential filter, $w(t) = \frac{1}{\tau}\exp\left(\frac{t}{\tau}\right)$, the ordinary differential equation (ODE)

$$\frac{\mathrm{d}}{\mathrm{d}t}\langle f\rangle = \frac{1}{\tau}\left(f - \langle f\rangle\right) \tag{7.16}$$

can be used to update the filtered value $\langle f\rangle$. Similarly the ODE

$$\frac{\mathrm{d}}{\mathrm{d}t}\langle\langle f\rangle\rangle = \frac{1}{\tau}\left(\left(f - \langle f\rangle\right)^2 - \langle\langle f\rangle\rangle\right) \tag{7.17}$$

can be used to apply a variance estimator $\langle\langle f\rangle\rangle$ with this particular kernel.

7.2.2 Atomic Data

Now that we have examined the example of mass density we can develop other consistent field estimators. For example, the expression for linear momentum density akin to Eq. (7.6),

$$\mathbf{p}(\mathbf{x}, t) = \sum_{I,\alpha} N_I(\mathbf{x}) \Delta_{I\alpha} m_\alpha \mathbf{v}_\alpha(t), \tag{7.18}$$

can be used together with the spatial version of the momentum balance,

$$\frac{\partial}{\partial t}\mathbf{p} = \nabla_{\mathbf{x}} \cdot \left(\boldsymbol{\sigma} - \frac{1}{\varrho}\mathbf{p} \otimes \mathbf{p}\right), \tag{7.19}$$

to derive the expression for the Cauchy stress $\boldsymbol{\sigma}$. Starting from the left-hand side of Eq. (7.19), at the nodes we obtain

$$\begin{aligned}
\frac{\partial}{\partial t}\mathbf{p}_I &= \sum_{I,\alpha} \frac{\partial}{\partial t}\left(\Delta_{I\alpha} m_\alpha \mathbf{v}_\alpha\right) = \sum_{I,\alpha}\left(\Delta_{I\alpha}\mathbf{f}_\alpha + m_\alpha \mathbf{v}_\alpha \frac{\partial \Delta_{I\alpha}}{\partial t}\right) \\
&= \sum_{I,\alpha,\beta} \Delta_{I\alpha}\mathbf{f}_{\alpha\beta} - \sum_{I,\alpha} m_\alpha \nabla_{\mathbf{x}} \Delta_{I\alpha} \cdot \mathbf{v}_\alpha \otimes \mathbf{v}_\alpha \\
&= \frac{1}{2}\sum_{I,\alpha,\beta}\left(\Delta_{I\alpha}\mathbf{f}_{\alpha\beta} - \Delta_{I\beta}\mathbf{f}_{\alpha\beta}\right) - \nabla_{\mathbf{x}} \cdot \sum_{I,\alpha} m_\alpha \mathbf{v}_\alpha \otimes \mathbf{v}_\alpha \Delta_{I\alpha},
\end{aligned} \tag{7.20}$$

where $\mathbf{f}_{\alpha\beta}$ is the portion of the total force on atom α due to atom β, such that $\mathbf{f}_\alpha = \sum_\beta \mathbf{f}_{\alpha\beta}$. As in Hardy's work [21, 47], we introduce the bond function

$$B_{I\alpha\beta} \equiv \int_0^1 \Delta_I(\lambda \mathbf{x}_{\alpha\beta} + \mathbf{x}_\beta - \mathbf{x}_I)\mathrm{d}\lambda, \tag{7.21}$$

such that

$$-\nabla_{\mathbf{x}} B_{I\alpha\beta} \cdot \mathbf{x}_{\alpha\beta} = \Delta_{I\alpha} - \Delta_{I\beta}, \tag{7.22}$$

where $\mathbf{x}_{\alpha\beta} \equiv \mathbf{x}_\alpha - \mathbf{x}_\beta$. By combining Eqs. (7.19), (7.20), and (7.22), we arrive at an expression for the Cauchy stress field,

$$\boldsymbol{\sigma}(\mathbf{x}, t) = -\frac{1}{2} \sum_{I,\alpha,\beta} \mathbf{f}_{\alpha\beta} \otimes \mathbf{x}_{\alpha\beta} B_{I\alpha\beta} N_I(\mathbf{x}) - \sum_{I,\alpha} m_\alpha \mathbf{w}_\alpha \otimes \mathbf{w}_\alpha \Delta_{I\alpha} N_I(\mathbf{x}), \tag{7.23}$$

where we define a relative atomic velocity

$$\mathbf{w}_\alpha = \mathbf{v}_\alpha - \sum_I \Delta_{I\alpha} \mathbf{v}_I \approx \mathbf{v}_\alpha - \frac{1}{V_I} \sum_I N_{I\alpha} \mathbf{v}_I. \tag{7.24}$$

As in [45], the projection form of Eq. (7.24) decouples the large-scale kinetic energy from the fine-scale, whereas, for the restriction form, this decomposition is only approximate.

A similar manipulation of the material-frame momentum density expression,

$$\mathbf{p}(\mathbf{X}, t) = \sum_{I,\alpha} N_I(\mathbf{X}) m_\alpha \mathbf{v}_\alpha \Delta_{I\alpha}, \tag{7.25}$$

where $\Delta_{I\alpha} = \Delta_I(\mathbf{X}_\alpha)$, within a material-frame momentum balance

$$\dot{\mathbf{p}} = \nabla_{\mathbf{X}} \cdot \mathbf{S}, \tag{7.26}$$

produces an expression for the first Piola–Kirchhoff stress,

$$\mathbf{S}(\mathbf{X}, t) = -\frac{1}{2} \sum_{I,\alpha,\beta} \mathbf{f}_{\alpha\beta}(t) \otimes \mathbf{X}_{\alpha\beta} B_{I\alpha\beta} N_I(\mathbf{X}). \tag{7.27}$$

A similar exercise can be done with the balance of energy, as shown in [35] and [36], by starting with a definition of nodal energy density,

$$\varrho_I e_I = \sum_\alpha \left(\frac{1}{2m_\alpha} \mathbf{p}_\alpha \cdot \mathbf{p}_\alpha + \phi_\alpha \right) \Delta_{I\alpha}, \tag{7.28}$$

where $\varrho e(\mathbf{x}, t) = \sum_I N_I(\mathbf{x}) \varrho_I(t) e_I(t)$. Here, we have partitioned the total potential energy Φ into separate contributions from each atom, ϕ_α, such that $\Phi = \sum_\alpha \phi_\alpha$. (For pair potentials ϕ_α is simply $\phi_\alpha = \frac{1}{2} \sum_\beta \phi_{\alpha\beta}$.) We require a direct relation between $\mathbf{f}_{\alpha\beta}$ and these individual atomic energies, specifically: $\mathbf{f}_{\alpha\beta} \equiv -\left\{ \frac{\partial \phi_\alpha}{\partial r_{\alpha\beta}} + \frac{\partial \phi_\beta}{\partial r_{\alpha\beta}} \right\} \frac{\mathbf{x}_{\alpha\beta}}{r_{\alpha\beta}}$, where $r_{\alpha\beta} = ||\mathbf{x}_{\alpha\beta}||$. Also, although energy density is

a primary field, i.e. is a conserved quantity associated with a balance law, we approximate ρe to conform to the more common convention of a per mass energy density. Using these expressions and relations within the Eulerian energy balance,

$$\varrho \frac{\partial e}{\partial t} = \nabla_{\mathbf{x}} \cdot (\boldsymbol{\sigma} \cdot \mathbf{v} - \varrho e \mathbf{v} - \boldsymbol{\varsigma}) \tag{7.29}$$

enables derivation of an expression for the heat flux[3] $\boldsymbol{\varsigma}$,

$$\boldsymbol{\varsigma} = -\sum_{I,\alpha,\beta} \left(\frac{\partial \phi_\beta}{\partial r_{\alpha\beta}} \frac{\mathbf{x}_{\alpha\beta}}{r_{\alpha\beta}} \cdot \mathbf{w}_\alpha \right) \mathbf{x}_{\alpha\beta} B_{I\alpha\beta} N_I(\mathbf{x}) + \sum_{I,\alpha} \left(\frac{1}{2} m_\alpha \mathbf{w}_\alpha \cdot \mathbf{w}_\alpha + \phi_\alpha \right) \Delta_{I\alpha} N_I(\mathbf{x}). \tag{7.30}$$

For the Lagrangian energy balance,

$$\rho \dot{e} = \mathbf{S} : \dot{\mathbf{F}} - \nabla_{\mathbf{X}} \cdot \mathbf{q}, \tag{7.31}$$

the resulting reference frame heat flux is

$$\mathbf{q} = -\sum_{I,\alpha,\beta} \left(\frac{\partial \phi_\beta}{\partial r_{\alpha\beta}} \frac{\mathbf{x}_{\alpha\beta}}{r_{\alpha\beta}} \cdot \mathbf{w}_\alpha \right) \mathbf{X}_{\alpha\beta} B_{I\alpha\beta} N_I(\mathbf{X}) \, . \tag{7.32}$$

Given the fundamental definitions of mass ρ and momentum density $\mathbf{p}$, we can define the velocity field $\mathbf{v}$ such that $\varrho \mathbf{v} = \mathbf{p}$. In our L^2 formalism:

$$\int_\Omega N_I \rho \mathbf{v} \, \mathrm{d}V = \int_\Omega N_I \mathbf{p} \, \mathrm{d}V \Longrightarrow \tag{7.33}$$

$$\int_\Omega N_I \sum_{J,\alpha} m_\alpha \delta(\mathbf{x} - \mathbf{x}_\alpha) N_J \, \mathrm{d}V \, \mathbf{v}_J = \int_\Omega N_I(\mathbf{x}) \sum_\alpha m_\alpha \mathbf{v} \delta(\mathbf{x} - \mathbf{x}_\alpha) \, \mathrm{d}V \Longrightarrow$$

$$\sum_{J,\alpha} \left[N_{I\alpha} m_\alpha N_{J\alpha} \right] \mathbf{v}_J = \sum_\alpha N_{I\alpha} m_\alpha \mathbf{v};$$

however, we choose to simply take the nodal velocities to be: $\mathbf{v}_I \equiv \mathbf{p}_I / \varrho_I$, and interpolate these values with the basis N_I. The corresponding displacement for node I is defined as

$$\mathbf{u}_I = \frac{1}{\varrho_I} \sum_{I\alpha} \Delta_{I\alpha} m_\alpha \mathbf{u}_\alpha = \frac{1}{\varrho_I} \sum_{I\alpha} \Delta_{I\alpha} m_\alpha \left(\mathbf{x}_\alpha - \mathbf{X}_\alpha \right) \tag{7.34}$$

[3] The term $\frac{\partial \phi_\beta}{\partial r_{\alpha\beta}} \frac{\mathbf{x}_{\alpha\beta}}{r_{\alpha\beta}}$ cannot be replaced with $-\mathbf{f}_{\alpha\beta}$, as is often done in the literature. This issue was examined by Admal and Tadmor [38], who determined that doing so also requires replacing $\mathbf{w}_\alpha$ with the average relative velocities of both atoms α and β, and modifying the internal energy density with an extra term that involves the difference between the velocities of the two atoms.

given reference configuration $\{\mathbf{X}_\alpha\}$. While this relation is exact for a Lagrangian analysis (as $\dot{\Delta}_{I\alpha} = 0$), with an Eulerian description an additional term involving $\mathbf{v}_\alpha$ breaks the correspondence between the displacement and its time-derivative, velocity. The displacement gradient $\mathbf{H} = \nabla_{\mathbf{X}}\mathbf{u}$, directly related to the deformation gradient $\mathbf{F} \equiv \nabla_{\mathbf{X}}\mathbf{x} = \mathbf{I} + \mathbf{H}$, can be derived via the basis

$$\mathbf{H} = \sum_I \mathbf{u}_I \otimes \nabla_{\mathbf{X}} N_I. \tag{7.35}$$

We can also define an expression for temperature T using the kinetic definition based on the principle of equipartition of energy [50, Sect. 6.4]:

$$3k_B T = \frac{2}{N} \sum_{\alpha=1}^{N} \langle k'_\alpha \rangle \tag{7.36}$$

i.e., an ensemble's internal energy equals twice its average fluctuating kinetic energy k'_α.[4] Along the lines of the derivation for the velocity $\mathbf{v}_I$, Eq. (7.33), we use Eq. (7.36) to obtain a temperature field

$$\sum_{J,\alpha} [N_{I\alpha} 3k_B N_{J\alpha}]\, T_J = \sum_\alpha N_{I\alpha} \underbrace{m_\alpha \mathbf{w}_\alpha \cdot \mathbf{w}_\alpha}_{2k'_\alpha}. \tag{7.37}$$

which we restrict to

$$T_I = \frac{1}{3k_B \sum_\alpha N_{I\alpha}} \sum_\alpha N_{I\alpha} m_\alpha \mathbf{w}_\alpha \cdot \mathbf{w}_\alpha = \frac{1}{3k_B} \sum_\alpha \Delta_{I\alpha} m_\alpha \mathbf{w}_\alpha \cdot \mathbf{w}_\alpha. \tag{7.38}$$

Our coarse-graining methodology can also be applied to diffusion/ionic conduction phenomena [3]. We start with the per-species mass density field akin to Eq. (7.6):

$$\varrho_I^{(a)} = \sum_{\alpha \in \mathscr{A}^{(a)}} m_\alpha \Delta_{I\alpha} \tag{7.39}$$

and associated flux

$$\mathbf{J}_I^{(a)} = \sum_{\alpha \in \mathscr{A}^{(a)}} m_\alpha \mathbf{v}_\alpha \Delta_{I\alpha} \tag{7.40}$$

[4] In statistical mechanics, temperature is defined in terms of the amount of phase space a system visits. We need to employ 'the "local equilibrium" and ergodic assumptions' in order to make the temperature a field variable and feasible to compute. We assume that the strict definition and ours coincide in the limit of large averaging volumes and long averaging times.

where $\mathscr{A}^{(a)}$ is the group of atoms that are of species a. Then the electrical current density $\mathbf{I}_0$ is the flux of ionic charge q_α

$$\begin{aligned}\mathbf{I}_0 &= \sum_{J,\alpha} q_\alpha \mathbf{v}_\alpha \Delta_{J\alpha} N_J = \sum_a z_a \mathbf{J}_a \\ &= \varrho\, z\, \mathbf{v} + \underbrace{\sum_a z^{(a)} \mathbf{J}^{(a)}}_{\mathbf{I}}\end{aligned} \tag{7.41}$$

split into convective, $\varrho z\mathbf{v}$, and diffusive, $\mathbf{I}$, components. Here $z^{(a)} = q^{(a)}/m^{(a)}$ is the valence of species a and

$$\varrho z = \sum_a \varrho^{(a)} z^{(a)} = \sum_{J,\alpha} q_\alpha \Delta_{J\alpha} N_J \tag{7.42}$$

is the total charge density. The diffusive ionic flux $\mathbf{I}$ satisfies the conservation equation

$$\varrho \dot{z} + \nabla_{\mathbf{x}} \cdot \mathbf{I} = 0 \tag{7.43}$$

by virtue of each of the species satisfying their respective mass conservation equations at the nodes and the fact that $z^{(a)}$ is constant:

$$\begin{aligned}\varrho \dot{z}_I = \frac{\mathrm{d}}{\mathrm{d}t} \sum_\alpha q_\alpha \Delta_{I\alpha} &= -\sum_\alpha q_\alpha \nabla_{\mathbf{x}} \Delta_{I\alpha} \cdot (\mathbf{v}_\alpha - \mathbf{v}) \\ &= -\nabla_{\mathbf{x}} \cdot \left[\sum_\alpha q_\alpha \left(\mathbf{v}_\alpha - \mathbf{v}\right) \Delta_{I\alpha} \right] = -\nabla_{\mathbf{x}} \cdot \mathbf{I}\end{aligned} \tag{7.44}$$

It is important to note that the material time derivative of the charge density $\dot{z}$ is with respect to the barycentric velocity $\mathbf{v}$ of the fluid [3].

7.2.3 Molecular Data

One can extend this same coarse-graining procedure to properties of molecular materials. As one such example, we consider electrical charge and the continuum quantities of electric field $\mathbf{E}$, electric displacement, $\mathbf{D}$, and polarization vector, $\mathbf{P}$. As discussed in [51], polarization quantifies the density of dipole moments in a dielectric material. Dipole moments can either be induced, as in non-polar molecules, or permanent, in polar molecules such as water. Here, we briefly develop expressions for $\mathbf{E}$, $\mathbf{D}$, and $\mathbf{P}$ using our upscaling formalism.

The (microscopic) electrostatic balance considering only atomic point charges is

$$\epsilon_0 \nabla_{\mathbf{x}} \cdot \mathbf{E} = \rho z^* \,, \tag{7.45}$$

where ϵ_0 is the vacuum permittivity and ρz is the microscopic charge density. The total charge density, ρz, is given by the summation of both free charges, q_α, over the group $\mathscr{A}_f$ of ions and charges on atoms, $q_{\beta m}$, belonging to molecules m:

$$\varrho z^* = \sum_{\alpha} q_\alpha \delta(\mathbf{x} - \mathbf{x}_\alpha) = \sum_{\alpha \in \mathscr{A}_f} q_\alpha \delta(\mathbf{x} - \mathbf{x}_\alpha) + \sum_{m,\beta} q_{\beta m} \delta(\mathbf{x} - (\mathbf{x}_m + \mathbf{x}_{\beta m})). \tag{7.46}$$

Following our coarse-graining methodology and employing a Taylor series expansion for the molecular charges around their (center-of-mass) coordinates $\mathbf{x}_m$

$$\epsilon_0 \int_\Omega N_I \nabla_{\mathbf{x}} \mathbf{E} \, \mathrm{d}V = \sum_{\alpha \in \mathscr{A}_f} N_{I\alpha} q_\alpha + \sum_{m,\beta \in \mathscr{M}_n} N_{Im} q_{\beta m} \tag{7.47}$$

$$+ \nabla_{\mathbf{x}} \cdot \underbrace{\left[\sum_{m,\beta \in \mathscr{M}_n} \left(-\mathbf{x}_{\beta m} N_{Im} + \frac{1}{2!} \mathbf{x}_{\beta m} \otimes \mathbf{x}_{\beta m} \cdot \nabla_{\mathbf{x}} N_{Im} + \ldots \right) q_{\beta m} \right]}_{\mathbf{P}} .$$

where we recognize the polarization vector $\mathbf{P}$ contains contributions from molecular dipole, $\sum_{\beta \in \mathscr{M}_m} q_{\beta m} \mathbf{x}_{\beta m}$; quadrupole, $\frac{1}{2!} \sum_{\beta \in \mathscr{M}_m} q_{\beta m} \mathbf{x}_{\beta m} \otimes \mathbf{x}_{\beta m}$; and higher moments. An integral form of the macroscopic Maxwell's equation result in $\nabla_{\mathbf{x}} \cdot \mathbf{D} = \zeta$, after defining $\mathbf{D} = \epsilon_0 \mathbf{E} + \mathbf{P}$, the electric displacement vector, and the coarse-grained charge related to the macroscopic free-charge density [51]

$$\zeta_I = \sum_{\alpha \in \mathscr{A}_f} N_{I\alpha} q_\alpha + \sum_{m,\beta \in \mathscr{M}_n} N_{Im} q_{\beta m} \,. \tag{7.48}$$

For molecules that are charge neutral, ζ_I reduces to $\sum_{I\alpha \in \mathscr{A}_f} N_{I\alpha} q_\alpha$.

Also, as noted in [51], the accuracy of $\mathbf{P}$ depends on the order of the polynomial used for the coarse-graining function. For example, if one uses a constant coarse-graining function, then only the dipole moments can be recovered. Likewise, if the basis is linear in $\mathbf{x}$, then the quadrupole moments may be computed. Lastly, the same methodology can be used to extract other quantities; for instance, by replacing the charge q_α in the expression for $\mathbf{P}$ in Eq. (7.47) with the mass m_α the moments of inertia can be extracted.

7.3 Coupling

As mentioned in the introduction, Sect. 7.1, in this section we will develop the basis for atom-to-continuum coupling simulation: (a) consistent upscaling/coarse-graining of the atomic state, (b) multiscale governing balances, (c) consistent

continuum surrogate models, and (d) atomistic control schemes. In Sect. 7.2 we have covered the first ingredient in detail which stands as useful tool in it own right. In this section we will discuss the remaining components of a fully coupled multiscale algorithm where $\Omega_{\text{FE}} \neq \emptyset$ and there is an interface, $\partial\Omega_{\text{FE}} \cap \partial\Omega_{\text{MD}}$, between the FE and MD regions.

Before developing the coupling methodology, we provide a brief overview of atomistic-to-continuum multiscale methods. This field is particularly rich in mechanical coupling schemes, and the interested reader is referred to the review article by Miller and Tadmor [52] for a more detailed description of the many strategies as well as references. Apparently the idea of using a coupled finite element model of material to alleviate the computational burden of computing atomic trajectories in regions that are expected to behave in a continuum fashion goes back to the early work of Kohlhoff et al. [53, 54]. Kohlhoff's application to fracture became one of the primary motivating examples for MD/FE mechanical coupling. Motivated by the same application, Tadmor, Ortiz et al. developed one of the most long-lived coupling algorithms: the quasicontinuum (QC) method [55]. Unlike in a strict domain-decomposition, QC takes the particles in the computation to transition between atoms driven by the interatomic potential and finite element nodes obeying a corresponding Cauchy–Born rule [56, 57]. In this method where primarily atomic domains transition to continuum, the particles become more widely spaced to reduce the burden of resolving all the atoms. Broughton et al. [58] derived a three-method algorithm based on hand-shaking regions, localized domains in which information is exchanged between different models which overlap in them, like in Kohlhoff's scheme, which combined tight-binding, MD, and FE. For each scale of exchange, a modified energy functional was derived incorporating contributions from both components. Another popular method is the bridging scale method of Wagner and Liu [45]. Their approach employs a hybrid Lagrangian incorporating the energy from both the atomic and continuum. Galerkin projection is used to partition the resulting forces and stresses between the two systems. Klein and Zimmerman [59] replaced standard finite elements with MLS and reproducing kernel bases for the continuum fields and to enable the multiscale information propagation, but also introduced a Cauchy–Born surrogate model for the continuum corrected near the boundary.

Since a continuum is an incomplete representation of an atomic system, other coupling methodologies use uncertainty quantification to exchange information between the two domains. In some cases, the goal is finding optimally consistent parameters for continuum closures using MD data [3, 60, 61]. In other cases, new closure model forms have been identified using MD samples to estimate a stochastic representation. This strategy has been employed in both off-line [62] and on-line [63] modes based on concurrency of the MD and continuum simulations.

7.3.1 Atomic Regulators

To effect the information transfer from continuum region to the atomistic system necessary for concurrent coupling, we have developed a variety of control/regulation strategies akin to the isokinetic thermostat [64] applied to a field of target values instead of a single system temperature. Both our method and the isokinetic thermostat are based on Gauss's principle of least constraint (GLC). In our application, GLC takes the form

$$\min_{\mathbf{f}_\alpha} \max_{\lambda_I} \underbrace{\left(\frac{1}{2} \sum_\alpha \|\mathbf{f}_\alpha - \mathbf{f}_\alpha^*\|^2 - \sum_I \lambda_I \dot{g}_I \right)}_{J}, \tag{7.49}$$

where $\mathbf{f}_\alpha^* \equiv -\partial_{\mathbf{x}_\alpha} \Phi$ are the unconstrained forces on atoms, g_I are the constraints dependent on atomic data, and λ_I are the associated Lagrange multipliers. It is clear from Eq. (7.49) that the principle is designed so that the Lagrange multipliers do the least work on the system necessary to enforce, the constraints. Also, note that the derivative of the constraint $\dot{g}_I$ is enforced not the constraint itself g_I. Our constraints g_I can be flux balances or field matching conditions analogous to Neumann or Dirichlet interface conditions and take the general form

$$g_I = \sum_\alpha N_{I\alpha} a_\alpha - A_I = 0, \tag{7.50}$$

where $a_\alpha = a(\mathbf{x}_\alpha, \mathbf{v}_\alpha)$ is a phase function corresponding to the nodal/continuum quantity A_I.

The (first order) optimality conditions arising from the extremization of the functional J in Eq. (7.49) recover the derivative of the constraint:

$$\partial_{\lambda_I} J = \dot{g}_I = \sum_\alpha N_{I\alpha} \dot{a}_\alpha - \dot{A}_I = \sum_\alpha N_{I\alpha} \left(\partial_{\mathbf{x}_\alpha} a_\alpha \cdot \mathbf{v}_\alpha + \partial_{\mathbf{v}_\alpha} a_\alpha \cdot \dot{\mathbf{v}}_\alpha \right) - \dot{A}_I = 0, \tag{7.51}$$

assuming a Lagrangian description ($\dot{N}_{I\alpha} = 0$), and the condition:

$$\partial_{\mathbf{f}_\alpha} J = \mathbf{f}_\alpha + \partial_{\mathbf{x}_\alpha} \Phi - \sum_I \lambda_I N_{I\alpha}\, \partial_{\mathbf{f}_\alpha} \dot{a}_\alpha = \mathbf{f}_\alpha + \partial_{\mathbf{x}_\alpha} \Phi - \sum_I \lambda_I N_{I\alpha}\, m_\alpha \partial_{\mathbf{v}_\alpha} a_\alpha = \mathbf{0}, \tag{7.52}$$

where we have used $m_\alpha \partial_{\mathbf{f}_\alpha} = \partial_{\dot{\mathbf{v}}_\alpha}$ from Newton's law: $m_\alpha \dot{\mathbf{v}}_\alpha = \mathbf{f}_\alpha$. We can rearrange Eq. (7.52) into an augmented form of Newton's law

$$m_\alpha \dot{\mathbf{v}}_\alpha = \mathbf{f}_\alpha = -\partial_{\mathbf{x}_\alpha} \Phi + \underbrace{\sum_I \lambda_I N_{I\alpha}\, m_\alpha \partial_{\mathbf{v}_\alpha} a_\alpha}_{\mathbf{f}_\alpha^\lambda} \tag{7.53}$$

which when we substitute it into the constraint, Eq. (7.51), gives a means of solving for λ_I:

$$\sum_{J,\alpha} \left[N_{I\alpha} \left(m_\alpha \| \partial_{\mathbf{v}_\alpha} a_\alpha \|^2 \right) N_{J\alpha} \right] \lambda_J = \dot{A}_I - \sum_\alpha N_{I\alpha} \left(\partial_{\mathbf{x}_\alpha} a_\alpha \cdot \mathbf{v}_\alpha - \partial_{\mathbf{v}_\alpha} a_\alpha \cdot \partial_{\mathbf{x}_\alpha} \Phi \right). \tag{7.54}$$

Now that we have a solution for λ_I, it is worth re-examining the structure of the problem. With the constraints g_I posed at nodes of the finite element mesh, the term $\sum_I \lambda_I N_{I\alpha}$ is the interpolation of the nodal field λ at the location of atom α. This is the conduit for propagation of continuum information in the form of a flux balance or field consistency to the atoms. Meanwhile, $\partial_{\mathbf{v}_\alpha} a_\alpha$ is strictly an atomic quantity and, as will be shown in detail, is related to conserved quantities. Hence, the correction $\mathbf{f}_\alpha^\lambda$ to the total force on the atom $\mathbf{f}_\alpha$ is a mixed-scale term incorporating aspects of both the small and large scales present in the problem and will introduce a correlation at the atomic level on the length-scale of the element size.

In our coupling schemes there are two instances of the nature of the constraint which are mutually exclusive at any particular node, like classical Dirichlet and Neumann conditions. For the first case of using the GLC framework to effect consistency between atomic data and a continuum field, we recognize the constraint

$$\sum_\alpha N_{I\alpha} \underbrace{m_\alpha \dot{\mathbf{v}}_\alpha}_{\dot{a}_\alpha} = \underbrace{\sum_J M_{IJ}^A \dot{\mathbf{p}}_J}_{\dot{A}_I}, \tag{7.55}$$

as an expression for the dynamics for a coarse-grained quantity, e.g. momentum. In general we apply M_{IJ}^A, the mass matrix over the atomic domain associated with quantity A, to obviate the need for applying a projection to the atomic information, i.e., the left-hand side of Eq. (7.55). On the other hand, in the case of enforcing a flux balance on the interface of the FE and MD regions, we tie the rate of change of a conserved quantity to the normal component of the associated flux, for instance

$$\sum_\alpha N_{I\alpha} \mathbf{f}_\alpha = \int_{\partial\Omega_{\mathrm{FE}}} N_I \boldsymbol{\sigma} \cdot \mathrm{d}\mathbf{A}. \tag{7.56}$$

This form is derivable from partitioning the global balance of the appropriate flux, see [10, 44] for more details.

These atomistic analogs of Dirichlet and Neumann boundary conditions can be applied simultaneously on disjoint sets of nodes. However, a consequence of our least squares formulation is that λ is, in general, non-zero throughout the domain. As a result, λ peaks at the MD-FE interface where the constraints are initially violated by uncorrected velocities and decays in an oscillatory fashion further into the MD domain. If this behavior is not desired, it is possible to localize λ near the MD boundary, but the method of localization is constraint-dependent. For the case of field-based constraints, Eq. (7.55), nodal λ_I's are only defined at nodes where the

constraint is imposed. The cost of this change is that the effect of the GLC affects the atomic domain an element away from the MD/FE boundary. Localization of the flux-based GLC approaches results in a similar effect, but results from row-sum lumping the matrix in Eq. (7.54) such that the global conservation balance is still respected [9]. Constraints involving time filtering can also be posed [44], and the formulation presented here is compatible with complex geometries, albeit at the cost of extra computational expense when localization is used [9].

Lastly, given that GLC derived regulators only control the derivative of the desired constraint it is necessary to set up initial conditions consistent with constraint. Unlike in the traditional FE framework, MD simulations typically need to be conditioned from some unlikely/unphysical state, e.g. a perfect lattice, to a representative sample of the desired ensemble. We find it is expedient to use a version of the velocity rescaling algorithm sometimes used as a thermostat to prepare an initial state for the subsequent dynamics controlled by GLC regulation. With

$$\sum_{\alpha} N_{I\alpha} a_{\alpha} = A_I, \tag{7.57}$$

we can pick a_α to be either the momentum $m_\alpha \mathbf{v}_\alpha$ or the kinetic energy $\frac{1}{2} m_\alpha \mathbf{v}_\alpha \cdot \mathbf{v}_\alpha$. To affect the change in a_α through $\mathbf{v}_\alpha^* = \sqrt[p]{s_\alpha}\mathbf{v}_\alpha$ where p is the power of $\mathbf{v}_\alpha$ in a_α, we construct the scaling field s_I interpolated to the atoms $s_\alpha = \sum_I N_{I\alpha} s_I$, which has the solution

$$\sum_{J,\alpha} \left[N_{I\alpha} a_\alpha N_{J\alpha} \right] s_J = A_I. \tag{7.58}$$

7.3.2 Mechanical Coupling

We now turn to the specific problem of mechanical coupling. In this case, the corresponding conserved quantities are atomic momentum $m_\alpha \mathbf{v}_\alpha$ and continuum momentum density $\mathbf{p} = \rho \mathbf{v}$. Using a Lagrangian description and the least-squares formalism introduced in Sect. 7.2.1:

$$\sum_J \left[\int_\Omega N_I \rho N_J \, \mathrm{d}V \right] \mathbf{v}_J = \int_{\Omega_{\mathrm{FE}}} N_I \rho \mathbf{v} \, \mathrm{d}V + \sum_\alpha N_{I\alpha} m_\alpha \mathbf{v}_\alpha \,, \tag{7.59}$$

we can solve for the velocity $\mathbf{v}$, instead of the momentum density $\mathbf{p}$, since the mass density field ρ is known and constant. A consistent decomposition of the left-hand side integral results in

$$\sum_J \underbrace{\left[\int_{\Omega_{\mathrm{FE}}} N_I \rho N_J \, \mathrm{d}V + \sum_\alpha N_{I\alpha} m_\alpha N_{J\alpha} \right]}_{M^V_{IJ}} \mathbf{v}_J = \int_{\Omega_{\mathrm{FE}}} N_I \rho \mathbf{v} \, \mathrm{d}V + \sum_\alpha N_{I\alpha} m_\alpha \mathbf{v}_\alpha \tag{7.60}$$

using an atomic definition of mass density $\rho_\alpha = \frac{m_\alpha}{V_\alpha}$ based on a consistent atomic volume/quadrature weight V_α such that $\int_{\Omega_{\text{MD}}} \mathrm{d}V = \sum_\alpha V_\alpha$. In the case of Eulerian frame equations, the shape function $N_{I\alpha}$ is now a function of time which reproduces the advective/convective fluxes; however, the atomic volume remains unknown but can be approximated by representing the atomic volume as a prolongation of a FE field consistent with $\int_{\Omega_{\text{MD}}} \mathrm{d}V = \sum_\alpha N_{I\alpha} V_I$ without modifying the governing equations. Hence, the dynamical equation governing the continuum velocity is

$$\sum_J \left[\int_{\Omega_{\text{FE}}} N_I \rho N_J \, \mathrm{d}V + \sum_\alpha N_{I\alpha} m_\alpha N_{J\alpha} \right] \dot{\mathbf{v}}_J = \int_{\Omega_{\text{FE}}} N_I \nabla_{\mathbf{X}} \cdot \mathbf{S} \, \mathrm{d}V + \sum_\alpha N_{I\alpha} \mathbf{f}_\alpha \quad (7.61)$$

after substituting the balance of linear momentum, Eq. (7.26), for the nodes, and Newton's law for the atoms. Before moving on to the influence of atomic control forces, several observations can be made. First, Eq. (7.61) is entirely consistent with either the finite element momentum equation or coarse-grained atomic momentum, Eq. (7.18), in the event only one type of region is present. Second, information propagates from the atomic system to the finite element region through the coarse-grained atomic force (the complementary flow of information was described in the previous section, Sect. 7.3.1).

To perform a coupled simulation, a final ingredient is required: a surrogate model for the interatomic-potential [65, 66] in the continuum region. Closures such as this are necessary in all continuum mechanics to account for the physics associated with the missing degrees of freedom and atomic interactions; in the present context they are assumed to be accurate for a limited regime of the possible atomic motion, e.g. nearly homogeneous deformation. It is important to note that the degree of consistency between the continuum closure and the true contributions from the atoms will impact the accuracy and sometimes the stability of the method. The Cauchy–Born model derived directly from the interatomic potential and the lattice [67, 68] and thermal models inferred from MD [61, 62] are examples of surrogate models particularly suited to MD/FE coupling.

For illustration of the present case, we introduce an elastic surrogate model which assumes a linear relationship between the stress tensor, $\mathbf{S}$, and (infinitesimal) strain:

$$\mathbf{S}(\mathbf{X}) \approx \mathbb{C} : \nabla_{\mathbf{X}} \mathbf{u}(\mathbf{x}) \approx \mathbb{C} : \sum_I \mathbf{u}_I \nabla_{\mathbf{X}} N_I, \quad (7.62)$$

with the fourth order elasticity tensor $\mathbb{C}$. After substituting this constitutive relationship into (7.61) and integrating by parts, we arrive at

$$\sum_J \left[\int_{\Omega_{\text{FE}}} N_I \rho N_J \, \mathrm{d}V + \sum_\alpha N_{I\alpha} m_\alpha N_{J\alpha} \right] \dot{\mathbf{v}}_J = -\sum_J \left[\int_{\Omega_{\text{FE}}} \nabla_{\mathbf{X}} N_I \, \mathbb{C} : \nabla_{\mathbf{X}} N_J \right] \mathrm{d}V \, \mathbf{u}_J + \int_{\partial\Omega_{\text{FE}}} N_I \mathbf{S} \cdot \mathrm{d}\mathbf{A} + \sum_\alpha N_{I\alpha} \mathbf{f}_\alpha, \quad (7.63)$$

which is completely prescribed except for the stress at the interface between the atomic and continuum domains, which we will address presently.

In order to couple the entire system, the continuum state must also influence the atoms. We accomplish this by using the constraint formalisms outlined in Sect. 7.3.1. The MD and FE sub-systems can be coupled either strongly by constraining the atomic forces based on the continuum velocity or weakly by using the continuum stress. Strong coupling uses the constraint:

$$\sum_{\alpha} N_{I\alpha}\mathbf{f}_{\alpha} = \sum_{J,\alpha} \left[N_{I\alpha} m_{\alpha} N_{J\alpha}\right] \dot{\mathbf{v}}_J. \tag{7.64}$$

Then Eq. (7.54) becomes

$$\sum_{J,\alpha} \left[N_{I\alpha} N_{J\alpha}\right] \boldsymbol{\lambda}_J = \sum_{J,\alpha} \left[N_{I\alpha} m_{\alpha} N_{J\alpha}\right] \dot{\mathbf{v}}_J + \sum_{\alpha} N_{I\alpha} \partial_{\mathbf{x}_{\alpha}} \Phi. \tag{7.65}$$

Similarly, weak coupling is derived using conservation of momentum for the total system,

$$\sum_{\alpha} \mathbf{f}_{\alpha} = -\int_{\partial\Omega_{\mathrm{FE}}} \mathbf{S} \cdot \mathrm{d}\mathbf{A}, \tag{7.66}$$

which after partitioning using the basis functions N_I implies

$$\sum_{\alpha} N_I \mathbf{f}_{\alpha}^{\lambda} = -\int_{\partial\Omega_{\mathrm{FE}}} N_I \mathbf{S} \cdot d\mathbf{A}. \tag{7.67}$$

The equation for $\boldsymbol{\lambda}$ is then

$$\sum_{J,\alpha} \left[N_{I\alpha} N_{J\alpha}\right] \boldsymbol{\lambda}_J = -\int_{\partial\Omega_{\mathrm{FE}}} N_I \mathbf{S} \cdot \mathrm{d}\mathbf{A}. \tag{7.68}$$

The last step in the derivation involves eliminating the unknown boundary flux in Eq. (7.63) by equating it with the force arising from the constraint, resulting in

$$\begin{aligned} &\sum_{J} \left[\int_{\Omega_{\mathrm{FE}}} N_I \rho N_J \, \mathrm{d}V + \sum_{\alpha} N_{I\alpha} m_{\alpha} N_{J\alpha} \right] \dot{\mathbf{v}}_J \\ &\quad = -\sum_{J} \left[\int_{\Omega_{\mathrm{FE}}} \nabla_{\mathbf{X}} N_I \, \mathbb{C} : \nabla_{\mathbf{X}} N_J \, \mathrm{d}V \right] \mathbf{u}_J - \sum_{\alpha} N_{I\alpha} \partial_{\mathbf{x}_{\alpha}} \Phi. \end{aligned} \tag{7.69}$$

In either case, the atomic dynamics result from

$$m_{\alpha} \dot{\mathbf{v}}_{\alpha} = -\partial_{\mathbf{x}_{\alpha}} \Phi + \sum_{I} N_{I\alpha} \lambda_I. \tag{7.70}$$

In many practical calculations, a layer of ghost atoms outside Ω_{MD} is used to exert forces to keep the unconstrained atoms within Ω_{MD}, refer to Fig. 7.1. The locations of the ghost atoms can be tied to the continuum displacement field, but in this case the forces the ghost atoms exert on the other atoms must be incorporated into the momentum conservation constraint. An alternative is simply to set the boundary stress based on the forces exerted by the ghost atoms, which also conserves momentum.

In fact there are a variety of means of coupling the atomistic and continuum motions and forces, but not all are inherently stable [69]. In particular, coupling the continuum to the atomistic flux, for instance the virial in mechanical coupling, generally leads to instabilities. Another issue that has received considerable attention [45] is how to handle the waves that are supported in the atomic region but cannot be transmitted to the continuum region due to the inherent mismatch in the dispersion characteristics of the two representations. Typically they are selectively damped out of the system [70] which violates overall energy conservation. This is another aspect of the incompleteness of the finite element representation.

7.3.3 *Thermal Coupling*

We now examine thermal coupling. With the definition of atomic temperature, Eq. (7.37), in hand, the least squares minimization procedure from Sect. 7.2.1 can be used to construct a finite element temperature field:

$$\sum_J \left[\int_\Omega N_I \rho c N_I \, \mathrm{d}V \right] T_J = \int_{\Omega_{\mathrm{FE}}} N_I \rho c T \, \mathrm{d}V + \sum_\alpha N_{I\alpha} m_\alpha \mathbf{w}_\alpha \cdot \mathbf{w}_\alpha \tag{7.71}$$

where the total fluctuating energy consistent with Eq. (7.37) appears on the right-hand side. The expression is a form of conservation of energy in absence of mechanical work, and hence we can reduce $\mathbf{w}_\alpha$ to $\mathbf{v}_\alpha$ and use a Lagrangian description of the material. Similar to the partition of the right-hand side into continuum and atomic domains, the left-hand side can be decomposed as

$$\sum_J \underbrace{\left[\int_{\Omega_{\mathrm{FE}}} N_I \rho c N_J \, \mathrm{d}V + 3k_B \sum_\alpha N_{I\alpha} N_{J\alpha} \right]}_{M^T_{IJ}} T_J = \int_{\Omega_{\mathrm{FE}}} N_I \rho c T \, \mathrm{d}V + \sum_\alpha N_{I\alpha} m_\alpha \mathbf{v}_\alpha \cdot \mathbf{v}_\alpha \tag{7.72}$$

using the Dulong–Petit law [71, Chap. 22] for the heat capacity

$$\rho c = \frac{3k_B}{V_\alpha} \tag{7.73}$$

of a classical solid material in conjunction with atomic quadrature weights V_α. For a system without a continuum region, this equation reduces to a projection of the temperature as in Eq. (7.37).

To reach the final form of the governing equation, we take the time derivative of Eq. (7.72):

$$\sum_J \left[\int_{\Omega_{\mathrm{FE}}} N_I \rho c N_J \, \mathrm{d}V + 3k_B \sum_\alpha N_{I\alpha} N_{J\alpha} \right] \dot{T}_J = \int_{\Omega_{\mathrm{FE}}} N_I \nabla \cdot \mathbf{q} \, \mathrm{d}V + 2 \sum_\alpha N_{I\alpha} \mathbf{v}_\alpha \cdot \mathbf{f}_\alpha. \tag{7.74}$$

Into this balance for the finite element temperature field we substitute Fourier's law for the referential heat flux

$$\mathbf{q}(\mathbf{X}) \approx -\boldsymbol{\kappa} \nabla_{\mathbf{X}} T = -\boldsymbol{\kappa} \sum_I T_I \nabla_{\mathbf{X}} N_I, \tag{7.75}$$

as a constitutive relationship for the heat flux $\mathbf{q}$ where $\boldsymbol{\kappa}$ is the thermal conductivity tensor. (Note that Fourier's law is not always an accurate surrogate model at small scales, see, e.g., [61].) Integrating the continuum right-hand side term of Eq. (7.74) by parts completes the derivation of the multiscale balance:

$$\sum_J \left[\int_{\Omega_{\mathrm{FE}}} N_I \rho c N_J \, \mathrm{d}V + 3k_B \sum_\alpha N_{I\alpha} N_{J\alpha} \right] \dot{T}_J = \sum_J \left[\int_{\Omega_{\mathrm{FE}}} \nabla N_I \cdot \boldsymbol{\kappa} \nabla N_J \, \mathrm{d}V \right] T_J + \int_{\partial \Omega_{\mathrm{FE}}} N_I \mathbf{q} \cdot \mathrm{d}\mathbf{A} + 2 \sum_\alpha N_{I\alpha} \mathbf{v}_\alpha \cdot \mathbf{f}_\alpha. \tag{7.76}$$

Now coupling can be imposed via constraints on the atomic force in the framework in Sect. 7.3.1. To maintain the consistency of the coarse-grained atomic temperature and the finite element temperature, their time derivatives are constrained to match using Eq. (7.50):

$$2 \sum_\alpha N_{I\alpha} \mathbf{v}_\alpha \cdot \mathbf{f}_\alpha = 3k_B \sum_{J,\alpha} N_{I\alpha} N_{J\alpha} \dot{T}_J. \tag{7.77}$$

In this case, the equation for the Lagrange multipliers, Eq. (7.54), becomes

$$\sum_{J,\alpha} \left[N_{I\alpha} \mathbf{v}_\alpha \cdot \mathbf{v}_\alpha N_{J\alpha} \right] \lambda_J = \frac{3k_B}{2} \sum_{J,\alpha} \left[N_{I\alpha} N_{J\alpha} \right] \dot{T}_J + \sum_\alpha N_{I\alpha} \partial_{\mathbf{x}_\alpha} \Phi \cdot \mathbf{v}_\alpha. \tag{7.78}$$

To conserve energy in the exchange between the continuum and atomic domains, the finite element boundary flux

$$\int_{\partial \Omega_{\mathrm{FE}}} N_I \mathbf{q} \cdot \mathrm{d}\mathbf{A} = -2 \sum_\alpha N_{I\alpha} \mathbf{v}_\alpha \cdot \mathbf{f}_\alpha^\lambda \tag{7.79}$$

is equated to the power due to the constraint force $\mathbf{f}_\alpha^\lambda$ from GLC. The governing equations for the FE and MD sub-systems are

$$\sum_J \left[\int_{\Omega_{\text{FE}}} N_I \rho c N_J \, \mathrm{d}V + 3k_B \sum_\alpha N_{I\alpha} N_{J\alpha} \right] \dot{T}_J \tag{7.80}$$
$$= \sum_J \left[\int_{\Omega_{\text{FE}}} \nabla N_I \cdot \boldsymbol{\kappa} \nabla N_J \, \mathrm{d}V \right] T_J - 2 \sum_\alpha N_{I\alpha} \mathbf{v}_\alpha \cdot \partial_{\mathbf{x}_\alpha} \Phi,$$
$$m_\alpha \dot{\mathbf{v}}_\alpha = -\partial_{\mathbf{x}_\alpha} \Phi + 2\mathbf{v}_\alpha \sum_I N_{I\alpha} \lambda_I. \tag{7.81}$$

When flux-based coupling is desired, conservation of energy is used to derive the constraint:

$$\partial_{\mathbf{x}_\alpha} \Phi \cdot \mathbf{v}_\alpha + \mathbf{f}_\alpha \cdot \mathbf{v}_\alpha = \mathbf{f}_\alpha^\lambda \cdot \mathbf{v}_\alpha = -\sum_I \int_{\partial\Omega_{\text{FE}}} N_I \mathbf{q} \cdot \mathrm{d}\mathbf{A}, \tag{7.82}$$

resulting in the governing equation for the Lagrange multipliers:

$$\sum_{J,\alpha} \left[N_{I\alpha} N_{J\alpha} \mathbf{v}_\alpha \right] \lambda_J = -\int_{\partial\Omega_{\text{FE}}} N_I \mathbf{q} \cdot \mathrm{d}\mathbf{A}, \tag{7.83}$$

when partitioned akin to Eq. (7.56), see [44]. However, in this case the flux is overcompensated for by our equipartition assumption, $3k_B T = m_\alpha \langle \mathbf{v}_\alpha \cdot \mathbf{v}_\alpha \rangle$, so the governing equations are

$$\sum_J \left[\int_{\Omega_{\text{FE}}} N_I \rho c N_J \, \mathrm{d}V + 3k_B \sum_\alpha N_{I\alpha} N_{J\alpha} \right] \dot{T}_J \tag{7.84}$$
$$= \sum_J \left[\int_{\Omega_{\text{FE}}} \nabla N_I \cdot \boldsymbol{\kappa} \nabla N_J \, \mathrm{d}V \right] T_J - 2 \sum_\alpha N_{I\alpha} \partial_{\mathbf{x}_\alpha} \Phi \cdot \mathbf{v}_\alpha + \sum_\alpha N_{I\alpha} \mathbf{v}_\alpha \cdot \mathbf{f}_\alpha^\lambda,$$
$$m_\alpha \dot{\mathbf{v}}_\alpha = -\partial_{\mathbf{x}_\alpha} \Phi + \mathbf{v}_\alpha \sum_I N_{I\alpha} \lambda_I. \tag{7.85}$$

Lastly, the required finite element heat fluxes can be computed using face-based quadrature schemes if the domain boundary aligns with the finite element faces, or using an approximate L^2 projection of the heat flux [44]. As a final comment, the thermostat force in the augmented Newton's equation (7.85) is of the recognizable velocity drag form common to many thermostats including the Langevin thermostat [72] but without the random force from the Mori–Zwanzig formalism.

7.3.4 Thermomechanical Coupling

The primary difference in developing a framework for thermomechanical coupling from the separate mechanical and thermal coupling we developed in the previous two sections is that the atomic momentum and temperature are no longer independent. The multiscale momentum balance (7.61) for the velocity is unchanged, but to derive the equation for temperature, we must start with the rate of change of the total energy:

$$\sum_J \left[\int_\Omega N_I \rho N_J \, \mathrm{d}V \right] \dot{e}_J = \int_{\Omega_{\mathrm{FE}}} N_I \left(\rho \dot{\varepsilon} + \rho \mathbf{v} \cdot \dot{\mathbf{v}} \right) \, \mathrm{d}V + \sum_\alpha N_{I\alpha} \left(m_\alpha \dot{\mathbf{v}}_\alpha + \partial_{\mathbf{x}_\alpha} \Phi \right) \cdot \mathbf{v}_\alpha \, . \tag{7.86}$$

We assume the total energy density e is the sum of internal energy density ε, which has thermal and elastic components, and coarse-scale kinetic energy[5]

$$\rho \dot{e} = \rho \dot{\epsilon} + \rho \mathbf{v} \cdot \dot{\mathbf{v}} = \rho c \dot{T} + \mathbf{S} \cdot \nabla_{\mathbf{X}\mathbf{v}} + \rho \mathbf{v} \cdot \dot{\mathbf{v}} \tag{7.87}$$

We can reduce Eq. (7.86) to

$$\begin{aligned} \sum_J \int_\Omega N_I \rho N_J \, \mathrm{d}V \, \dot{\varepsilon}_J &= \int_{\Omega_{\mathrm{FE}}} N_I \rho \dot{\varepsilon} \, \mathrm{d}V - \int_{\Omega_{\mathrm{MD}}} N_I \rho \mathbf{v} \cdot \dot{\mathbf{v}} \, \mathrm{d}V \\ &\quad + \sum_\alpha N_{I\alpha} \left(m_\alpha \dot{\mathbf{v}}_\alpha + \partial_{\mathbf{x}_\alpha} \Phi \right) \cdot \mathbf{v}_\alpha \\ &= \int_{\Omega_{\mathrm{FE}}} N_I \rho \dot{\varepsilon} \, \mathrm{d}V \\ &\quad + \sum_\alpha N_{I\alpha} \underbrace{\left(m_\alpha \mathbf{v}_\alpha \cdot \dot{\mathbf{v}}_\alpha - \sum_J N_{J\alpha} \rho_J \mathbf{v}_J \cdot \dot{\mathbf{v}}_J V_\alpha \right)}_{\dot{k}'_\alpha} + \partial_{\mathbf{x}_\alpha} \Phi \cdot \mathbf{v}_\alpha \end{aligned} \tag{7.88}$$

using the atomic quadrature based on weights V_α and making the particular definition of the fluctuating kinetic energy k'_α. Note that our use of inexact projections/restrictions leads to k'_α not being identified with our previous definition of the thermal energy $\frac{1}{2} m_\alpha \mathbf{w}_\alpha \cdot \mathbf{w}_\alpha$ from Sect. 7.2. Using Eq. (7.61), the coupled multi-scale equations for the nodal velocities, $\mathbf{v}_I$ and temperatures, T_I are

$$M^V_{IJ} \dot{\mathbf{v}}_J = - \int_{\Omega^{\mathrm{FE}}} \nabla_{\mathbf{X}} N_I \cdot \mathbf{S} \, \mathrm{d}V + \int_{\partial \Omega_{\mathrm{FE}}} N_I \mathbf{S} \cdot \, \mathrm{d}\mathbf{A} + \sum_\alpha N_{I\alpha} \mathbf{f}_\alpha , \tag{7.89}$$

[5] This a common assumption that neglects, for example, interactions between the thermal and the coarse-scale mechanical energy related to thermal expansion at the macro-scale.

$$M_{IJ}^T \dot{T}_J = -\int_{\Omega_{\mathrm{FE}}} \nabla_{\mathbf{X}} N_I \cdot \mathbf{q}\, \mathrm{d}V + \int_{\partial\Omega_{\mathrm{FE}}} N_I \mathbf{q} \cdot \mathrm{d}\mathbf{A} + \sum_\alpha N_{I\alpha} \left(\dot{k}'_\alpha + \partial_{\mathbf{x}_\alpha} \Phi \cdot \mathbf{v}_\alpha \right). \tag{7.90}$$

As in the previous two sections, we need surrogate models for the first Piola–Kirchhoff stress $\mathbf{S}$ and referential heat flux $\mathbf{q}$. A good model for the former is the Cauchy–Born model based on a quasi-harmonic free energy detailed in [68].

To form the appropriate constraints, we begin with the global conservation of momentum and (total) energy:

$$\frac{\mathrm{d}}{\mathrm{d}t} \left(\sum_\alpha m_\alpha \mathbf{v}_\alpha + \int_{\Omega_{\mathrm{FE}}} \mathbf{p}\, \mathrm{d}V \right) = \sum_\alpha \mathbf{f}_\alpha + \int_{\partial\Omega_{\mathrm{FE}}} \mathbf{S}\, \mathrm{d}\mathbf{A} = \int_{\partial\Omega} \mathbf{S}\, \mathrm{d}\mathbf{A} \tag{7.91}$$

$$\begin{aligned} \frac{\mathrm{d}}{\mathrm{d}t} \left(\sum_\alpha m_\alpha e_\alpha + \int_{\Omega^{\mathrm{FE}}} \rho e\, \mathrm{d}V \right) &= \sum_\alpha (\mathbf{f}_\alpha + \partial_{\mathbf{x}_\alpha} \Phi) \cdot \mathbf{v}_\alpha + \int_{\partial\Omega_{\mathrm{FE}}} (\mathbf{v} \cdot \mathbf{S} - \mathbf{q}) \cdot \mathrm{d}\mathbf{A} \\ &= \int_{\partial\Omega} (\mathbf{v} \cdot \mathbf{S} - \mathbf{q}) \cdot \mathrm{d}\mathbf{A} \end{aligned} \tag{7.92}$$

which we reduce and partition to form:

$$\mathbf{g}_I^V = \sum_\alpha N_{I\alpha} \mathbf{f}_\alpha - \int_{\partial\Omega \setminus \partial\Omega_{\mathrm{FE}}} N_I \mathbf{S}\, \mathrm{d}\mathbf{A} = \mathbf{0} \tag{7.93}$$

$$g_I^T = \sum_\alpha N_{I\alpha} (\mathbf{f}_\alpha + \partial_{\mathbf{x}_\alpha} \Phi) \cdot \mathbf{v}_\alpha - \int_{\partial\Omega \setminus \partial\Omega_{\mathrm{FE}}} N_I (\mathbf{v} \cdot \mathbf{S} - \mathbf{q}) \cdot \mathrm{d}\mathbf{A} = 0 \tag{7.94}$$

As previously discussed, the augmented force in the MD component is $\mathbf{f}_\alpha = -\partial_{\mathbf{x}_\alpha} \Phi + \mathbf{f}_\alpha^\lambda$ where in this case $\mathbf{f}_\alpha^\lambda$ takes the form

$$\mathbf{f}_\alpha^\lambda = -\sum_I N_I \left(\boldsymbol{\lambda}_I^V + \lambda_I^T \mathbf{v}_\alpha \right), \tag{7.95}$$

with a vector $\boldsymbol{\lambda}_I^V$ and scalar λ_I^T Lagrange multipliers similar to system-wide momentum and temperature control found in [73]. This modified force is substituted into each constraint to obtain the following block symmetric system of equations for $\boldsymbol{\lambda}_I^V$ and λ_I^T:

$$\sum_{J,\alpha} [N_{I\alpha} N_{J\alpha}] \boldsymbol{\lambda}_I^V + \sum_{J,\alpha} [N_{I\alpha} \mathbf{v}_\alpha N_{J\alpha}] \lambda_J^T = -\sum_\alpha N_{I\alpha} \partial_{\mathbf{x}_\alpha} \Phi - \int_{\partial\Omega_{\mathrm{MD}}} N_I \mathbf{S}\, \mathrm{d}\mathbf{A} \tag{7.96}$$

$$\sum_{J,\alpha} [N_{I\alpha} \mathbf{v}_\alpha N_{J\alpha}] \cdot \boldsymbol{\lambda}_I^V + \sum_{J,\alpha} [N_{I\alpha} \mathbf{v}_\alpha \cdot \mathbf{v}_\alpha N_{J\alpha}] \lambda_J^T = -\int_{\partial\Omega \setminus \partial\Omega_{\mathrm{FE}}} N_I (\mathbf{v} \cdot \mathbf{S} - \mathbf{q}) \cdot \mathrm{d}\mathbf{A} \tag{7.97}$$

7.4 Examples

In this section we demonstrate the utility of the methods we have developed with selected applications of the coarse-graining, Sect. 7.2, and coupling, Sect. 7.3, methodologies.

7.4.1 Inclusion

With this example we demonstrate the utility and versatility of our coarse-graining methods by examining the simple case of insertion of an oversized inclusion within a constrained lattice. Figure 7.2a shows the face-centered cubic (fcc) gold lattice 20×20 unit cells on a side and 3 unit cells thick in the out-of-plane direction (4800 atoms, lattice parameter of 4.08 Å). Periodic boundary conditions are used in all directions. We employ a Lennard-Jones [74, 75] pair potential smoothly truncated at distance of about 5.46 Å. We expand the center region of 4×4 unit cells by 0.5 % and hold the atoms in this inclusion region fixed, while the outer material is allowed to relax via energy minimization.

Figure 7.2a shows the atomic displacement magnitudes, with the largest displacements occurring at the inclusion corners. Figure 7.2b shows the coarse-graining of these displacements onto a 10×10 element mesh that overlays the atomic system. Here, we use the mesh's own interpolation function as the coarse-graining operator. The resulting displacement field has similar features to the atomic one, albeit with a noticeably lower peak magnitude.

Figures 7.2c–e illustrates the use of a localization kernel at each node to coarse-grain the atomic displacements, where the kernel differs from the mesh interpolation function N_I. Here, we use a quartic polynomial that depends on the radial distance from the node's position, with its maximum value at the node and smoothly reaching zero at a distance just over the cutoff of the potential, 6 Å (as recommended in [4]). Comparing Fig. 7.2b and Fig. 7.2c, which use the same 10×10 mesh, we observe that the field coarseness remains the same, but the peak value is somewhat higher for the kernel-averaged system. Figures 7.2d, e reveal how use of a successively refined mesh (20×20 and 40×40, respectively) improves the resolution and fidelity of the coarse-grained field.

This comparison shows the advantage of using independent localization kernels for coarse-graining—in fact the kernel size could vary throughout the domain and be tied to atomic density or field gradients. Use of kernels enables the calculation of robust averages and continuous fields that correspond to the local continuum limits [49] for an arbitrary degree of mesh resolution. In contrast, exclusive use of the mesh's interpolation function would produce either a field with converged values but coarse features (for a mesh with large element size), or one with fine features but spatially fluctuating, non-converged values (for a mesh with small element size).

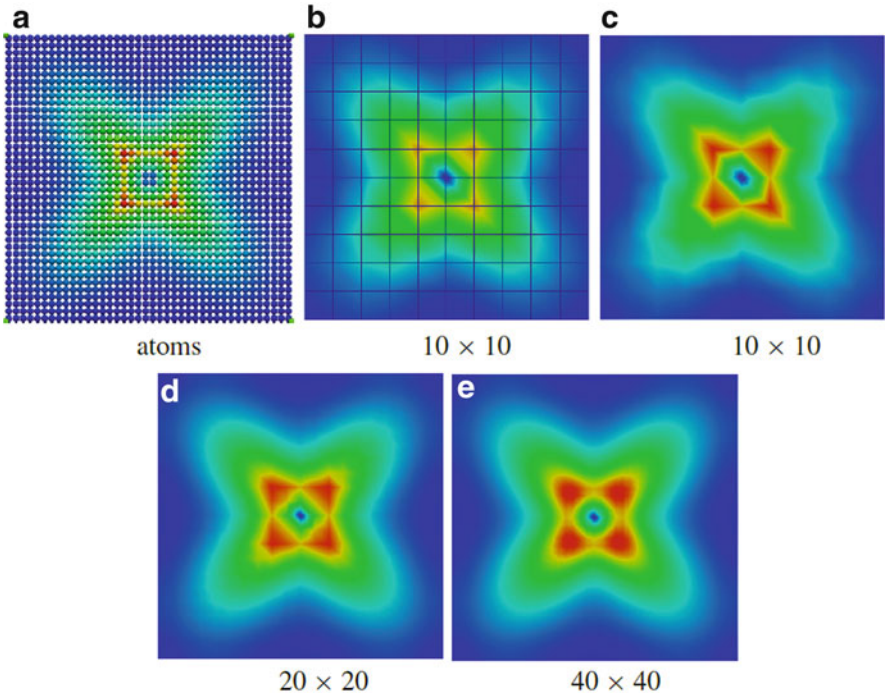

Fig. 7.2 Displacement magnitude, $\|\mathbf{u}\|$, for insertion of an oversized inclusion in fcc gold. (**a**) Atoms colored by atomic displacements. (**b**) Coarse-graining on a 10×10 mesh using interpolation functions. (**c**)–(**e**) Coarse-graining using localization kernels on 10×10, 20×20 and 40×40 meshes. Here, $\|\mathbf{u}\|$ ranges from 0 (*blue*) to 0.05 Å for the atomic system, or 0.037 Å for the coarse-grained systems (*red*)

We also used our coarse-graining methods to calculate the continuum stress fields for this inclusion problem. Figure 7.3 shows the $\boldsymbol{\sigma}_{11}$ and $\boldsymbol{\sigma}_{12}$ fields using the finely resolved 40×40 mesh with localization kernels. The resulting fields are smoothly varying and appear to be consistent with expectations of continuum mechanics.

7.4.2 J-Integral

Coarse-graining methods enable the use of continuum fields to estimate other metrics defined within continuum theory, e.g. configurational forces. Based on the seminal work by Eshelby [76] and developed in the context of fracture mechanics by Rice [77], the J-integral is a path independent contour or surface integral (in two- or three-dimensions, respectively) that measures the energetic driving force on a defect. The J-integral is commonly used in numerical simulations of continuum

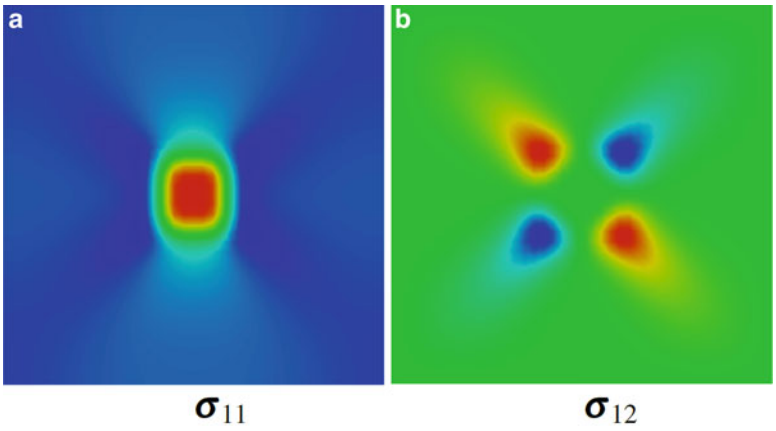

Fig. 7.3 (**a**) σ_{11} and (**b**) σ_{12} for insertion of an oversized inclusion in fcc gold. Coarse-graining is performed using localization kernels on a 40 × 40 mesh. Stress values range from −0.59 to 3.71 GPa for σ_{11} and from −0.85 to 0.85 GPa for σ_{12} (*blue-to-red*)

mechanical deformation, such as the finite element method, to indicate when a critical loading state has been achieved that will result in crack propagation.

Jones and Zimmerman [5] discussed past efforts to estimate the J-integral at the atomic scale, and proposed use of the coarse-graining methods covered in this chapter as a means to ensure consistency with linear elastic fracture mechanics (LEFM), and to preserve the path independence of the J-integral. In that work, the J-integral expression for a isothermal, equilibrium material is given as

$$\mathbf{J} = \int_{\partial\Omega} \left(W\mathbf{I} - \mathbf{H}^T\mathbf{S} \right) \mathrm{d}\mathbf{A}, \tag{7.98}$$

where W is the material frame internal energy density, and $\mathbf{H}$ and $\mathbf{S}$ have already been defined as the displacement gradient and 1st Piola–Kirchhoff stress fields, respectively. In [5], it was shown that W and $\mathbf{S}$ exhibited thermodynamic consistency (i.e., $\mathbf{S} = \partial W/\partial \mathbf{F}$), thereby ensuring that the J-integral around a closed region with a smooth motion is zero and consequently that $\mathbf{J}$ is path independent for arbitrary contours around regions that contain singularities such as crack tips.

Figure 7.4a shows the S_{22} stress field for a single crack in a cylinder composed of the same LJ gold used in the inclusion example. Here, displacements are imposed on atoms within an outer annulus of the cylinder in accordance with the LEFM solution for a mode I loaded crack tip. Details about this simulation are given in [5]. We note that this stress field contains the same characteristic pattern as predicted by the LEFM solution. Figure 7.4b plots the J-integral for a square contour that encircles the crack tip (shown clearly in Fig. 7.4a) as a function of the square of the applied stress intensity factor, K_I. In LEFM theory, J_1 for this configuration should be proportional to K_I^2, as shown by the straight, black line in the figure. We see

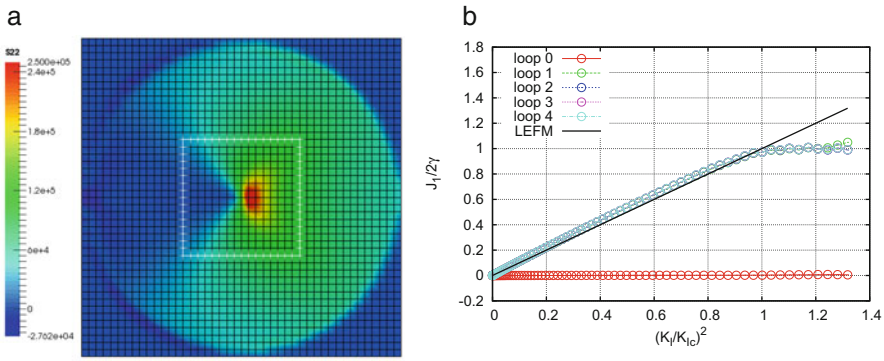

Fig. 7.4 (**a**) The S_{22} stress (units in *bars*) from a coarse-grained estimate. A contour loop and the FE interpolation grid are also shown. (**b**) The calculated J-integral for the single crack configuration showing path independence. J-integral values are normalized by twice the surface energy of the Lennard-Jones system and the loading parameter K_I by the corresponding critical value K_{Ic}

that for a set of concentric loops of varying size, our estimation follows this trend up to the point when crack propagation begins, $J_1 = 2\gamma$, thereby confirming path independence of the J-integral. Discrepancies from exact linearity may be due to the anisotropic and non-linear aspects of the LJ potential, as well as the non-ideal aspects of the crack face geometry. We also observe that for a loop that does not enclose the crack tip singularity (loop 0), $J_1 = 0$, as expected.

In [6], this approach was expanded to treat systems at a finite (i.e., non-zero) temperature. In this case, the J-integral is given by the expression

$$\mathbf{J} = \int_{\partial\Omega} \left(\Psi\mathbf{I} - \mathbf{F}^T\mathbf{S}\right) \mathrm{d}\mathbf{A}, \tag{7.99}$$

where Ψ is the Helmholtz free energy density, a function of both deformation gradient $\mathbf{F}$ and temperature T. At finite temperature, Ψ has contributions from both internal (strain) energy and entropy [68]. In [6], this entropic term was determined by a local harmonic (LH) approximation that requires calculation of a simplified dynamical matrix that neglects coupling between atoms. Details on this method are given in [6], along with an analysis that shows the LH approximation to closely correspond with a more exact calculation of free energy using thermodynamic integration up to significant temperatures ($\lesssim$ 400 K) for substantial amounts of uniaxial and volumetric strains. Application of Eq. (7.99) to the single crack tip geometry showed that although the J_1 dependence on applied stress intensity factor changes slightly due to thermal stresses that arise in the heated system, path independence at a given temperature is maintained [6].

7.4.3 *Polarization Field of a Double Layer*

The methods presented in this chapter can be used to investigate inhomogeneous and anisotropic phenomena which occur at the atomic scale. An interesting example is the electric double layer, in which an ionic solution covers a charged surface, resulting in a screening layer of oppositely charged ions attracted from the solution. Double layers are important in many applications, ranging from electrokinetic flows in micro- and nano-fluidic devices to energy storage devices including batteries and super-capacitors. Despite their ubiquity, they are still poorly understood because experimentally it is difficult to resolve the length-scales over which they develop, and the configuration for realistic systems is too complex for a purely theoretical treatment. However, molecular dynamics studies [2, 78–80] have provided insights into double layer structure, and the coarse-graining theories for atoms and molecules enable a deeper understanding of the important physics.

In this example, we model a box of salt water using molecular dynamics periodic in two directions and constrained by a uniform force field in the third to mimic a nano-channel geometry. A uniform electric field is also applied in this direction to account for a potential drop across the channel. When this happens, a structured layer of solvent and solute particles formed, followed slightly further from the wall by a diffuse layer in which the solute remains at elevated concentrations but no significant structure is present. Figure 7.5 shows this structure at the boundary. Coarse-graining the atoms enables a continuum density field to be post-processed, as shown in Fig. 7.6. The densities are important because they enable the calculation of the electric field and electric potential throughout the domain. These quantities allow us to determine the structure of the condensed layer, how far it extends away from the boundary, and how much charge the double layer can store.

We can understand the double layer structure more deeply by quantifying its electrical properties [51] using the methods outlined in Sect. 7.2.3. Molecular coarse-graining elucidates the degree to which the solvent is aligned with the electric field. Figure 7.7 shows the strong polarization present in the structured layer to be more than an order of magnitude greater than the bulk values. More importantly, the polarization is beyond the level at which a constant relative permittivity is a useful description, implying that the physics cannot be understood without appeal to the atomic nature of matter. However, resolving the boundary region allows us

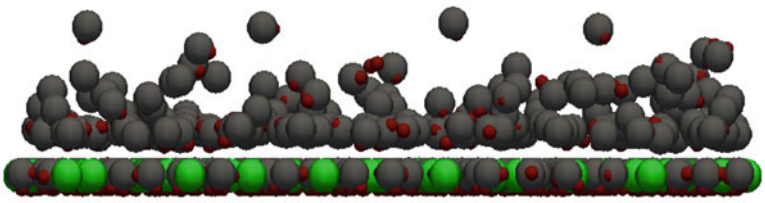

Fig. 7.5 Structure of ions and molecules near the boundary. *Grey* denotes oxygen, *red* hydrogen, and *green* counter-ions. Reproduced from [79] with permission

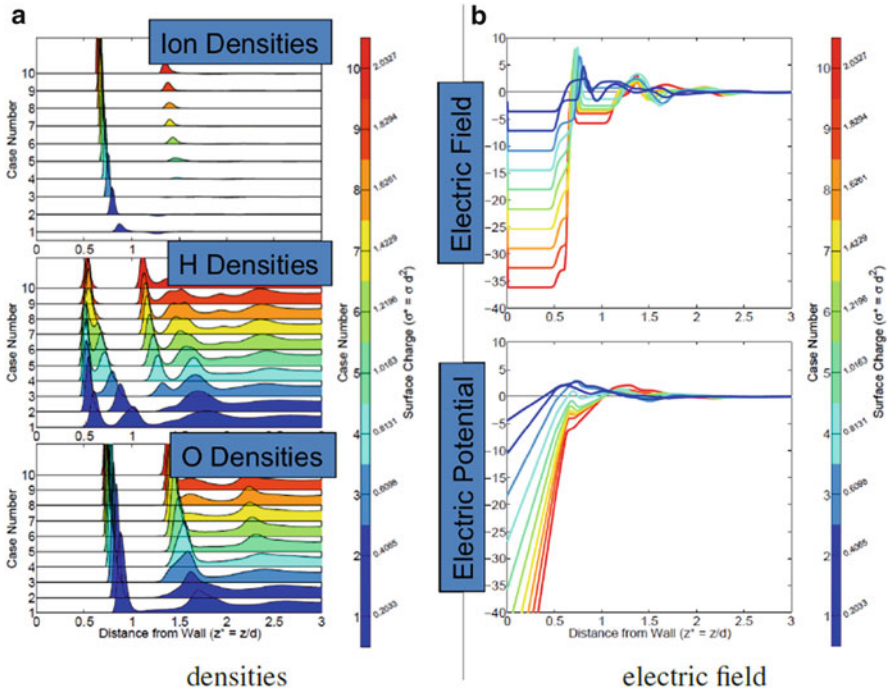

Fig. 7.6 Fields obtained from nanochannel simulations: (**a**) densities associated with different types of atoms using atomic coarse-graining, and (**b**) the electric field and electric potential from Gauss' law using the coarse-grained charge density. Reproduced from [79] with permission

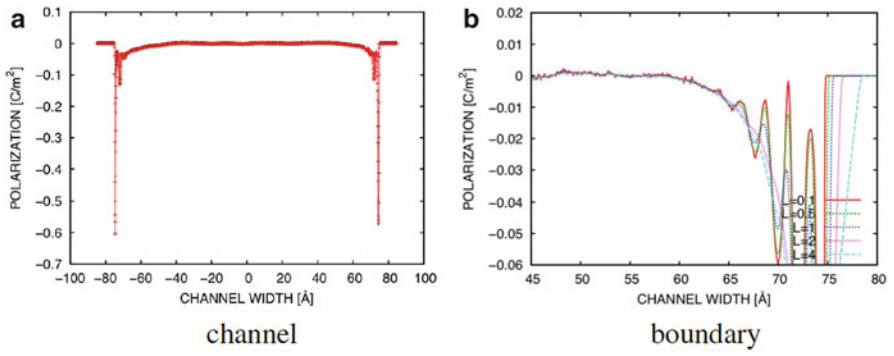

Fig. 7.7 Polarization profile in a nanochannel: throughout the entire channel (**a**) and near the boundary (**b**). Reproduced from [51] with permission

to determine over exactly what sub-domain is the atomic description necessary. By comparing fields resulting from different coarse-graining length-scales, we can identify continuum behavior where the field is independent of length-scale. And, conversely, in regions where the length-scale is important, a continuum description will be inadequate.

7.4.4 *Surface Relaxation*

Surface relaxation due to interatomic forces and lack of full coordination shells is a phenomenon that can only be approximated in finite element simulation and not in a fully predictive manner. In this demonstration we model the surface relaxation of a cube of Ni nominally 38.72 Å on a side both as a fully atomic system and a mechanically coupled atomic/FE system. We use the embedded atom model (EAM) potential [81–83] for the interatomic forces in Ni and either (a) the associated Cauchy–Born model for the elastic stresses or (b) a cubic elastic model with $C_{11} = 261\,\text{GPa}$, $C_{12} = 151\,\text{GPa}$, and $C_{44} = 132\,\text{GPa}$.

The results from the all atom simulation in Fig. 7.8a show significant displacement as the cube relaxes from a perfect lattice arrangement. The maximum displacements $|u_1|, |u_2| \approx 0.2\,\text{Å}$ occur at the corners of the material. As can be seen from Fig. 7.8b,c the coupled simulation with the Cauchy–Born and the significantly less computationally intensive cubic elastic surrogate models,[6] respectively,

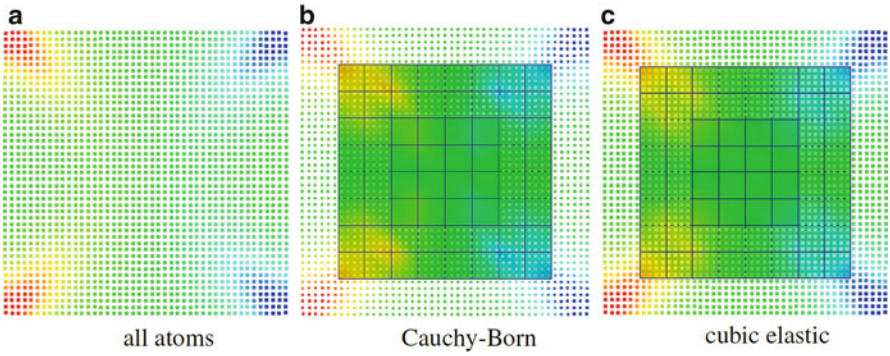

Fig. 7.8 Displacement in the x-direction: (**a**) all atoms, (**b**) CB coupled, (**c**) cubic elastic coupled. Range $\pm$ 0.2 Å

[6]The cost of the molecular statics solution is proportional to the number of atoms times the number of neighbors per atoms, while the cost of the Cauchy–Born solution is proportional to the number of elements times the number of integration points per element times the number of neighbors per atoms, while the cost of the Cauchy-Born cubic elastic solution is proportional to merely the product of the number of elements and the number of integration points per element.

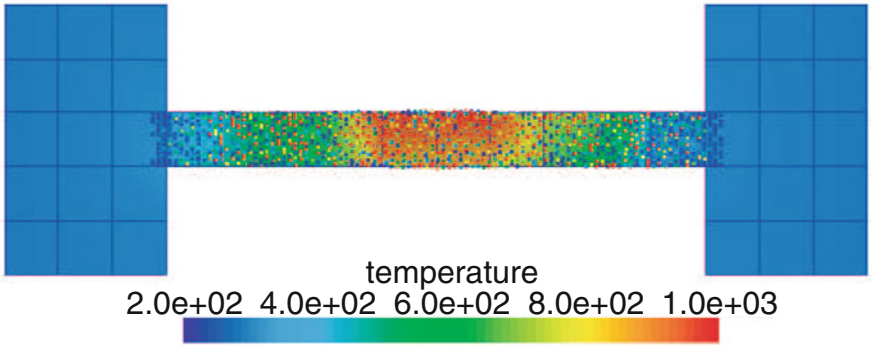

Fig. 7.9 Metallic CNT embedded in an FE mesh showing phonon temperature near the beginning of the heating phase, $t = 10$ ps. Reproduced from [10] with permission

reproduce the all atom displacement field with considerable fidelity. We attribute this result to the fact that the coupled scheme preserves momentum and that in this zero temperature simulation the field of displacements is smooth on the scale of the mesh.

7.4.5 Laser Heating of a Carbon Nanotube

In this example a metallic (8,8) armchair carbon nanotube (CNT), 12.6 nm long, is suspended by embedding its ends in solid graphite, see Fig. 7.9 and [10], and heated with a shaped laser pulse directly heating the CNT's electron gas. We use the Tersoff potential [84, 85] to model the CNT. The graphite substrate is modeled with a continuum with the same thermal properties as the CNT. The exposed surface of the reservoirs and the tube are insulated by the air so that no heat crosses those boundaries and the remaining surfaces of the reservoirs are fixed at a constant temperature of 300 K. The electronic heat capacity has a temperature dependency: $c_e = \gamma\theta_e$ with $\gamma = 1.5\,\mathrm{J/m^3\,K^2}$, and the electronic heat conductivity $k_e = L\sigma\theta_e$ is estimated with the Franz–Wiedemann law with $L\sigma = 2.443 \times 10^{-3}\,\mathrm{W/m\,K^2}$. In addition to temperature dependence of the electron heat capacity and conductivity, the measured form of the electron–phonon exchange for CNTs [86] is highly nonlinear in temperature, $g = h(\theta_e - \theta_p)^5$ with $h = 3.7 \times 10^4\,\mathrm{W/m^3\,K^5}$. Also, the fact that the CNT lattice is not space filling creates no algorithmic difficulties since its contribution directly and fully determines the phonon temperature in the regions where there are atoms. In these elements all the effects of the phonon constitutive model are removed. To offset the larger fluctuations associated with basis functions with few atoms in their support we employ a time-filter, with characteristic time-scale $\tau = 0.01$ ps.

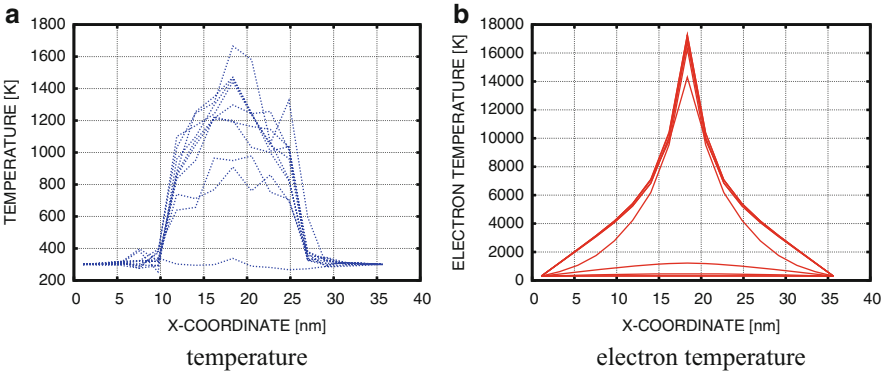

Fig. 7.10 Sequence of temperature (**a**) and electron temperature (**b**) profiles along the axis of the CNT. Reproduced from [10] with permission

The electron system of the CNT interacts with a focused radiation source that has a power input of $1.6 \times 10^{-12} \exp(-(x_1^2 + x_2^2)/(0.1\,[\text{nm}])^2)\,\text{W/m}^3$. We turn on this localized source for 50 ps and then allow the system to relax. The sequence of temperature profiles along the axis of the tube in Fig. 7.10 shows very localized electron and relatively diffuse phonon temperatures in correspondence with their diffusivities. These profiles through the axis of the CNT extend into FE regions without atoms; in the reservoir regions, we see a distinct change in slope due to the reservoirs' higher thermal mass, especially for the phonons. As the experiments [87] demonstrate, we expect mixed ballistic/diffusive transport in the CNT, which is modeled entirely by the MD. This mixed harmonic/enharmonic transport must transition to purely diffusive heat flux at the CNT-reservoir boundary, given the nature of the coupling. The large scale oscillations that start to become apparent at about $t = 40$ ps in Fig. 7.11 indicate that the input energy to electrons eventually excites a strong fundamental mode resonance [88, 89] which can be directly observed in Fig. 7.12.

7.5 Conclusion

We have presented the framework for the ATC methods available in LAMMPS together with illustrative examples. In contrast to other coupling methods, ATC has the distinct advantage of treating the full possibilities of thermal transport at the nanoscale since its inception [45] and provides a generalized framework of consistent multiscale balances, coarse graining, and control schemes that are applicable to a wide range of multiphysics problems. In its present state of development it is particularly suited to warm, slow processes like: predicting the growth of large nanostructures via vapor deposition, simulating the steep gradation

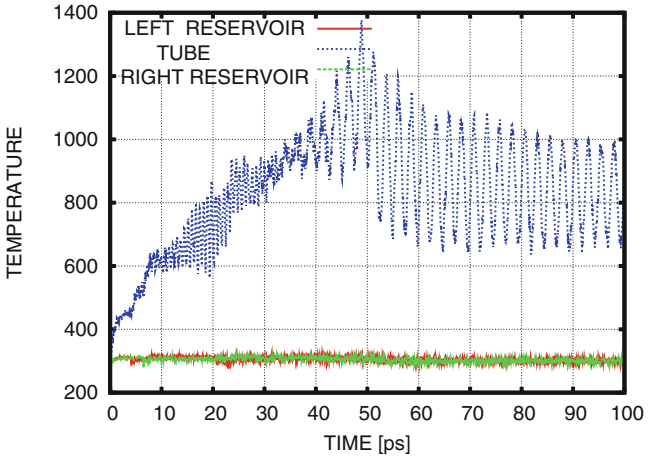

Fig. 7.11 Evolution of average temperatures of the two explicitly modeled reservoirs and the CNT. Reproduced from [10] with permission

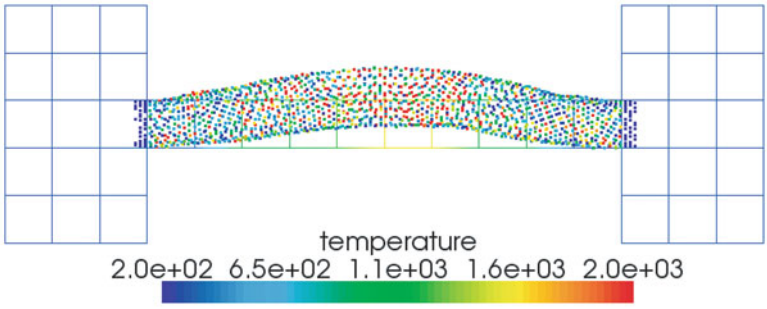

Fig. 7.12 Fundamental mode excited by focused irradiation. The atoms and the mesh are both colored by the phonon temperature. Reproduced from [10] with permission

from an electrical double layer to a bulk fluid, and modeling the deformation of polycrystalline materials with complex grain boundary structure. In general, the method is appropriate for systems with characteristic sizes reaching micrometers containing large regions of regular behavior interacting through structures requiring atomic detail. We have laid the groundwork of treating the ubiquitous problem of spurious wave reflection in the shock and dynamic regimes [70] in the ATC framework but this topic has also been an area of intense development by other researchers; see, for example, the review by Miller and Tadmor [90] and the seminal paper by Wagner and Liu [45].

The scope of the theory presented and the particular version of the methodology have not been presented elsewhere and we hope this chapter serves as a concise and coherent overview of the work we have done in the upscaling and coupling arenas. Full-fledged fluid coupling is notably absent from our exposition mainly due to the complexity introduced by treating open systems.

Acknowledgements Thanks to Greg Wagner (Northwestern University), Mike Parks (Sandia), Steve Plimpton (Sandia), Aidan Thompson (Sandia), Paul Crozier (Sandia) for assistance in developing the methods that reside in the ATC package:

http://lammps.sandia.gov/doc/fix_atc.html

Sandia is a multiprogram laboratory managed and operated by Sandia Corporation, a wholly owned subsidiary of Lockheed Martin Corporation, for the U.S. Department of Energy's National Nuclear Security Administration under contract No. DE-AC04-94AL85000.

References

1. J.A. Templeton, R.E. Jones, J.W. Lee, J.A. Zimmerman, B.M. Wong, A long-range electric field solver for molecular dynamics based on atomistic-to-continuum modeling. J. Chem. Theory Comput. **7**(6), 1736–1749 (2011)
2. J.W. Lee, J.A. Templeton, K.K. Mandadapu, J.A. Zimmerman, Comparison of molecular and primitive solvent models for electrical double layers in nanochannels. J. Chem. Theory Comput. **9**, 3051–3061 (2013)
3. R.E. Jones, D.K. Ward, J.A. Templeton, Spatial resolution of the electrical conductance of ionic fluids using a Green-Kubo method. J. Chem. Phys. **141**(18), 184110 (2014)
4. J.A. Zimmerman, E.B. Webb III, J.J. Hoyt, R.E. Jones, P.A. Klein, D.J. Bammann, Calculation of stress in atomistic simulation. Model. Simul. Mater. Sci. Eng. **12**(4), S319 (2004)
5. R.E. Jones, J.A. Zimmerman, The construction and application of an atomistic J-integral via hardy estimates of continuum fields. J. Mech. Phys. Solids **58**(9), 1318–1337 (2010)
6. R.E. Jones, J.A. Zimmerman, J. Oswald, T. Belytschko, An atomistic J-integral at finite temperature based on hardy estimates of continuum fields. J. Phys. Condens. Matter **23**(1), 015002 (2011)
7. J.A. Zimmerman, R.E. Jones, The application of an atomistic J-integral to a ductile crack. J. Phys. Condens. Matter **25**(15), 155402 (2013)
8. R.E. Jones, J.A. Templeton, T.W. Rebold, Simulated real-time detection of a small molecule on a carbon nanotube cantilever. J. Comput. Theor. Nanosci. **8**(8), 1364–1384 (2011)
9. J.A. Templeton, R.E. Jones, G.J. Wagner, Application of a field-based method to spatially varying thermal transport problems in molecular dynamics. Model. Simul. Mater. Sci. Eng. **18**(8), 085007 (2010)
10. R.E. Jones, J.A. Templeton, G.J. Wagner, D. Olmsted, N.A. Modine, Electron transport enhanced molecular dynamics for metals and semi-metals. Int. J. Numer. Methods Eng. **83**(8–9), 940–967 (2010)
11. M.H. Ulz, K.K. Mandadapu, P. Papadopoulos, On the estimation of spatial averaging volume for determining stress using atomistic methods. Model. Simul. Mater. Sci. Eng. **21**(1), 15010–15024 (2013)
12. G.I. Barenblatt, *Scaling, Self-Similarity, and Intermediate Asymptotics: Dimensional Analysis and Intermediate Asymptotics*, vol. 14 (Cambridge University Press, Cambridge, 1996)
13. LAMMPS : Large-scale Atom/Molecular Massively Parallel Simulator, Sandia National Laboratories (2015), http://lammps.sandia.gov
14. R.J.E. Clausius, On a mechanical theorem applicable to heat. Philos. Mag. **40**, 122–127 (1870)
15. J.C. Maxwell, On reciprocal figures, frames and diagrams of forces. Trans. R. Soc. Edinb. **XXVI**, 1–43 (1870)
16. J.H. Irving, J.G. Kirkwood, The statistical mechanical theory of transport processes. IV. the equations of hydrodynamics. J. Chem. Phys. **18**(6), 817–829 (1950)
17. W. Noll, Die herleitung der grundgleichungen der thermomechanik der kontinua aus der statistischen mechanik. J. Ration. Mech. Anal. **4**(5), 627–646 (1955)

18. R.B. Lehoucq, A.V. Lilienfeld-Toal, Translation of Walter Noll's "Derivation of the fundamental equations of continuum thermodynamics from statistical mechanics". J. Elast. **100**(1–2), 5–24 (2010)
19. D.H. Tsai, The virial theorem and stress calculation in molecular dynamics. J. Chem. Phys. **70**, 1375–1382 (1979)
20. P. Schofield, J.R. Henderson, Statistical mechanics of inhomogeneous fluids. Proc. R. Soc. Lond. A **379**, 231–240 (1982)
21. R.J. Hardy, Formulas for determining local properties in molecular-dynamics simulations: shock waves. J. Chem. Phys. **76**(1), 622–628 (1982)
22. J.F. Lutsko, Stress and elastic constants in anisotropic solids: molecular dynamics techniques. J. Appl. Phys. **64**(3), 1152–1154 (1988)
23. J.S. Rowlinson, B. Widom, *Molecular Theory of Capillarity* (Clarendon Press, Oxford, 1989)
24. K.S. Cheung, S. Yip, Atomic-level stress in an inhomogeneous system. J. Appl. Phys. **70**(10), 5688–5690 (1991)
25. J. Cormier, J.M. Rickman, T.J. Delph, Stress calculation in atomistic simulations of perfect and imperfect solids. J. Appl. Phys. **89**(1), 99–104 (2001)
26. M. Zhou, D.L. McDowell, Equivalent continuum for dynamically deforming atomistic particle systems. Philos. Mag. A **82**, 2547–2574 (2002)
27. M. Zhou, A new look at the atomic level virial stress: on continuum-molecular system equivalence. Proc. R. Soc. Lond. Ser. A **459**, 2347–2392 (2003)
28. A.I. Murdoch, On the microscopic interpretation of stress and couple stress. J. Elast. **71**, 105–131 (2003)
29. F. Costanzo, G.L. Gray, P.C. Andia, On the notion of average mechanical properties in md simulation via homogenization. Model. Simul. Mater. Sci. Eng. **12**, S333–S345 (2004)
30. F. Costanzo, G.L. Gray, P.C. Andia, On the definitions of effective stress and deformation gradient for use in md: Hill's macro-homogeneity and the virial theorem. Int. J. Eng. Sci. **43**, 533–555 (2005)
31. P.C. Andia, F. Costanzo, G.L. Gray, A lagrangian-based continuum homogenization approach applicable to molecular dynamics simulation. Int. J. Solids Struct. **42**, 6409–6432 (2005)
32. P.C. Andia, F. Costanzo, G.L. Gray, A classical mechanics approach to the determination of the stress-strain response of particle systems. Model. Simul. Mater. Sci. Eng. **14**, 741–757 (2006)
33. M. Zhou, Thermomechanical continuum representation of atomistic deformation at arbitrary size scales. Proc. R. Soc. Lond. Ser. A **461**, 3437–3472 (2006)
34. A.I. Murdoch, A critique of atomistic definitions of the stress tensor. J. Elast. **88**, 113–140 (2007)
35. E.B. Webb III, J.A. Zimmerman, S.C. Seel, Reconsideration of continuum thermomechanical quantities in atomic scale simulations. Math. Mech. Solids **13**, 221–266 (2008)
36. J.A. Zimmerman, R.E. Jones, J.A. Templeton, A material frame approach for evaluating continuum variables in atomistic simulations. J. Comput. Phys. **229**(6), 2364–2389 (2010)
37. N.C. Admal, E.B. Tadmor, A unified interpretation of stress in molecular systems. J. Elast. **100**, 63–143 (2010)
38. N.C. Admal, E.B. Tadmor, Stress and heat flux for arbitrary multibody potentials: a unified framework. J. Chem. Phys. **134**, 184106 (2011)
39. R.J. Hardy, A.M. Karo, Stress and energy flux in the vicinity of a shock front, in *Shock Compression of Condensed Matter. Proceedings of the American Physical Society Topical Conference* (Elsevier, Amsterdam, 1990), pp. 161–164
40. R.J. Hardy, S. Root, D.R. Swanson, Continuum properties from molecular simulations, in *12th International Conference of the American-Physical-Society-Topical-Group on Shock Compression of Condensed Matter. AIP Conference Proceedings*, vol. 620, Pt. 1 (American Institute of Physics, Melville, 2002), pp. 363–366
41. F. Rizzi, R.E. Jones, B.J. Debusschere, O.M. Knio, Uncertainty quantification in md simulations of concentration driven ionic flow through a silica nanopore. I. Sensitivity to physical parameters of the pore. J. Chem. Phys. **138**(19), 194104 (2013)
42. F. Rizzi, R.E. Jones, B.J. Debusschere, O.M. Knio, Uncertainty quantification in MD simulations of concentration driven ionic flow through a silica nanopore. II. Uncertain potential parameters. J. Chem. Phys. **138**(19), 194105 (2013)

43. A. Donev, J.B. Bell, A.L. Garcia, B.J. Alder, A hybrid particle-continuum method for hydrodynamics of complex fluids. Multiscale Model. Simul. **8**(3), 871–911 (2010)
44. G.J. Wagner, R.E. Jones, J.A. Templeton, M.L. Parks, An atomistic-to-continuum coupling method for heat transfer in solids. Comput. Methods Appl. Mech. Eng. **197**(41), 3351–3365 (2008)
45. G.J. Wagner, W.K. Liu, Coupling of atomistic and continuum simulations using a bridging scale decomposition. J. Comput. Phys. **190**(1), 249–274 (2003)
46. P. Lancaster, K. Salkauskas, Surfaces generated by moving least squares methods. Math. Comput. **37**, 141–158 (1981)
47. S. Root, R.J. Hardy, D.R. Swanson, Continuum predictions from molecular dynamics simulations: shock waves. J. Chem. Phys. **118**(7), 3161–3165 (2003)
48. W.K. Liu, S. Jun, Y.F. Zhang, Reproducing kernel particle methods. Int. J. Numer. Methods Fluids **20**(8–9), 1081–1106 (1995)
49. M.H. Ulz, S.J. Moran, Optimal kernel shape and bandwidth for atomistic support of continuum stress. Model. Simul. Mater. Sci. Eng. **21**(8), 085017 (2013)
50. K. Huang, *Statistical Mechanics*, 2nd edn. (Wiley, New York, 1987)
51. K.K. Mandadapu, J.A. Templeton, J.W. Lee, Polarization as a field variable from molecular dynamics simulations. J. Chem. Phys. **139**, 054115 (2013)
52. R.E. Miller, E.B. Tadmor, A unified framework and performance benchmark of fourteen multiscale atomistic/continuum coupling methods. Model. Simul. Mater. Sci. Eng. **17**(5), 053001 (2009)
53. S. Kohlhoff, S. Schmauder, A new method for coupled elastic-atomistic modelling, in *Atomistic Simulation of Materials* (Springer, New York, 1989), pp. 411–418
54. S. Kohlhoff, P. Gumbsch, H.F. Fischmeister, Crack propagation in bcc crystals studied with a combined finite-element and atomistic model. Philos. Mag. A **64**(4), 851–878 (1991)
55. E.B. Tadmor, M. Ortiz, R. Phillips, Quasicontinuum analysis of defects in solids. Philos. Mag. A **73**(6), 1529–1563 (1996)
56. E. Weinan, P. Ming, Cauchy–Born rule and the stability of crystalline solids: static problems. Arch. Ration. Mech. Anal. **183**(2), 241–297 (2007)
57. J.L. Ericksen, On the Cauchy–Born rule. Math. Mech. Solids **13**(3–4), 199–220 (2008)
58. J.Q. Broughton, F.F. Abraham, N. Bernstein, E. Kaxiras, Concurrent coupling of length scales: methodology and application. Phys. Rev. B **60**(4), 2391 (1999)
59. P.A. Klein, J.A. Zimmerman, Coupled atomistic–continuum simulations using arbitrary overlapping domains. J. Comput. Phys. **213**(1), 86–116 (2006)
60. F. Rizzi, M. Salloum, Y.M. Marzouk, R.G. Xu, M.L. Falk, T.P. Weihs, G. Fritz, O.M. Knio, Bayesian inference of atomic diffusivity in a binary Ni/Al system based on molecular dynamics. SIAM Multi. Model. Simul. **9**, 486–512 (2011)
61. M. Salloum, J. Templeton, Inference and uncertainty propagation of atomistically-informed continuum constitutive laws, part 1: Bayesian inference of fixed model forms. Int. J. Uncertain Quantif. **4**(2), 151–170 (2014)
62. M. Salloum, J. Templeton, Inference and uncertainty propagation of atomistically-informed continuum constitutive laws, part 2: genereralized continuum models based on gaussian processes. Intl. J. Uncertain. Quantif. **4**(2), 171–184 (2014)
63. M. Salloum, K. Sargsyan, R. Jones, B. Debusschere, H.N. Najm, H. Adalsteinsson, A stochastic multiscale coupling scheme to account for sampling noise in atomistic-to-continuum simulations. Multiscale Model. Simul. **10**(2), 550–584 (2012)
64. D.J. Evans, W.G. Hoover, B.H. Failor, B. Moran, A.J.C. Ladd, Nonequilibrium molecular dynamics via gauss's principle of least constraint. Phys. Rev. A **28**(2), 1016 (1983)
65. F. Rizzi, H.N. Najm, B.J. Debusschere, K. Sargsyan, M. Salloum, H. Adalsteinsson, O.M. Knio, Uncertainty quantification in md simulations. part I: forward propagation. Multiscale Model. Simul. **10**(4), 1428 (2012)
66. F. Rizzi, H.N. Najm, B.J. Debusschere, K. Sargsyan, M. Salloum, H. Adalsteinsson, O.M. Knio, Uncertainty quantification in md simulations. part II: Bayesian inference of force-field parameters. Multiscale Model. Simul. **10**(4), 1460 (2012)

67. P. Steinmann, A. Elizondo, R. Sunykm, Studies of validity of the Cauchy-Born rule by direct comparison of continuum and atomistic modelling. Model. Simul. Mater. Sci. Eng. **15**, S271–S281 (2007)
68. C.J. Kimmer, R.E. Jones, Continuum constitutive models from analytical free energies. J. Phys. Condens. Matter **19**(32), 326207 (2007)
69. W. Ren, Analytical and numerical study of coupled atomistic-continuum methods for fluids. J. Comput. Phys. **227**(2), 1353–1371 (2007)
70. R.E. Jones, C.J. Kimmer, Efficient non-reflecting boundary condition constructed via optimization of damped layers. Phys. Rev. B **81**(9), 094301 (2010)
71. N.W. Ashcroft, N.D. Mermin, *Solid State Physics* (Brooks-Cole, Belmont, 1976)
72. T. Schneider, E. Stoll, Molecular-dynamics study of a three-dimensional one-component model for distortive phase transitions. Phys. Rev. B **17**, 1302–1322 (1978)
73. T. Ikeshoji, B. Hafskjold, Non-equilibrium molecular dynamics calculation of heat conduction in liquid and through liquid-gas interface. Mol. Phys. **81**(2), 251–261 (1994)
74. J.E. Lennard-Jones, The determination of molecular fields I. From the variation of the viscosity of a gas with temperature. Proc. R. Soc. Lond. **106A**, 441 (1924)
75. J.E. Lennard-Jones, The determination of molecular fields II. From the equation of state of a gas. Proc. R. Soc. Lond. **106A**, 463 (1924)
76. J.D. Eshelby, The force on an elastic singularity. Philos. Trans. R. Soc. Lond. A **244**(877), 87–112 (1951)
77. J.R. Rice, A path independent integral and approximate analysis of strain concentration by notches and cracks. J. Appl. Mech. **35**(2), 379–386 (1968)
78. R. Qiao, N.R. Aluru, Ion concentrations and velocity profiles in nanochannel electroosmotic flows. J. Chem. Phys. **118**(10), 4692–4701 (2003)
79. J.W. Lee, R.H. Nilson, J.A. Templeton, S.K. Griffiths, A. Kung, B.M. Wong, Comparison of molecular dynamics with classical density functional and poisson–boltzmann theories of the electric double layer in nanochannels. J. Chem. Theory Comput. **8**(6), 2012–2022 (2012)
80. J.W. Lee, A. Mani, J.A. Templeton, Atomistic and molecular effects in electric double layers at high surface charges. Langmuir **31**(27), 7496–7502 (2015)
81. M.S. Daw, M.I. Baskes, Semiempirical, quantum mechanical calculation of hydrogen embrittlement in metals. Phys. Rev. Lett. **50**(17), 1285 (1983)
82. M.S. Daw, M.I. Baskes, Embedded-atom method: derivation and application to impurities, surfaces, and other defects in metals. Phys. Rev. B **29**(12), 6443 (1984)
83. S.M. Foiles, M.I. Baskes, M.S. Daw, Embedded-atom-method functions for the fcc metals Cu, Ag, Au, Ni, Pd, Pt, and their alloys. Phys. Rev. B **33**(12), 7983 (1986)
84. J. Tersoff, New empirical-approach for the structure and energy of covalent systems. Phys. Rev. B **37**(12), 6991–7000 (1988)
85. J. Tersoff, Modeling solid-state chemistry: interatomic potentials for multicomponent systems. Phys. Rev. B **39**, R5566–R5568 (1989)
86. T. Hertel, R. Fasel, G. Moos, Charge-carrier dynamics in single-wall carbon nanotube bundles: a time-domain study. Appl. Phys. A **75**(4), 449–465 (2002)
87. J. Wang, J.-S. Wang, Carbon nanotube thermal transport: ballistic to diffusive. Appl. Phys. Lett. **88**(11), 111909 (2006)
88. E.H. Feng, R.E. Jones, Equilibrium thermal vibrations of carbon nanotubes. Phys. Rev. B **81**(12), 125436 (2010)
89. E.H. Feng, R.E. Jones, Carbon nanotube cantilevers for next-generation sensors. Phys. Rev. B **83**(19), 195412 (2011)
90. R.E. Miller, E.B. Tadmor, A unified framework and performance benchmark of fourteen multiscale atomistic/continuum coupling methods. Model. Simul. Mater. Sci. Eng. **17**(5), 053001 (2009)